A targeted 3D EM and correlative microscopy method using SEM array tomography

Agnes Burel[1], Marie-Thérèse Lavault[1], Clément Chevalier[1,4], Helmut Gnaegi[2], Sylvain Prigent[1], Antonio Mucciolo[3], Stéphanie Dutertre[1], Bruno M. Humbel [3], Thierry Guillaudeux[1], and Irina Kolotuev[1, 3*]

[1] University of Rennes 1, UMS Biosit, MRic, Rennes, France

[2] Diatome SA, Helmstrasse 1, 2560 Nidau, Switzerland

[3] University of Lausanne, EM Facility, Lausanne, Switzerland

[4] Present address: ULB, Center for microscopy and molecular imaging, Gosselies, Belgium

* Corresponding author: irina.kolotueva@unil.ch

Keywords: correlative light and electron microscopy (CLEM), array tomography, volume reconstruction, model organisms, *C. elegans, Drosophila,*

Abstract

Using electron microscopy to localize rare cellular events or structures in complex tissue is challenging. Correlative light and electron microscopy procedures have been developed to link fluorescent protein expression with ultrastructural resolution. Here, we present an optimized scanning electron microscopy (SEM) workflow for volumetric Array Tomography for asymmetric samples and model organisms (*Caenorhabditis elegans*, *Drosophila melanogaster, Danio rerio*). We modified a diamond knife to simplify serial section arrays acquisition with minimal artifacts. After array acquisition, we transfer the arrays to a glass coverslip or silicon wafer support. Using light microscopy, we rapidly screen the arrays for initial recognition of global anatomical features (organs or body traits). Then, using SEM, we perform an in-depth study of the cells and/or organs of interest. Our manual and automatic data acquisition strategies make 3D data acquisition and correlation simpler and more precise than do alternative methods. This method can be used to address questions in cell and developmental biology that require the efficient identification of a labeled cell or organelle.

Abbreviations

AT – Array Tomography

CLEM – Correlative Light and Electron Microscopy

EM – Electron Microscopy

FIB – Focused Ion Beam

FLM – Fluorescent Light Microscopy

HPF – High-Pressure Freezing

QFS – Quick Freeze Substitution

RCs – Ring Canals

ROI – Region of Interest

SEM - Scanning Electron Microscopy

SBF - Serial Block Face

TEM – Transmission Electron Microscopy

Introduction

Imaging methods aid the analysis and understanding of biological processes. Advanced fluorescent light microscopy (FLM) techniques can answer questions about the localization, dynamics, and interactions of proteins in various organs and cell structures. Genetically encoded fluorescence tools enable the study of live processes. However, many cellular processes cannot be fully visualized, due to the insufficient resolution of fluorescent labeling and the lack of visible reference structures within the cell. Much higher resolution of cellular components can be obtained with electron microscopy, which is crucial for the analysis of cellular ultrastructure. Recently, cellular ultrastructure has been directly correlated with a fluorescence signal using correlative light and electron microscopy (CLEM; Caplan et al., 2011; Muller-Reichert and Verkade, 2014).

Serial section transmission electron microscopy (TEM), as well as tilt series combined with electron tomography, have been the primary tools for reconstructing ultrastructure within a defined volume. These methods have significantly contributed to our current understanding of the local 3D organization of biological samples (White et al., 1986; Bumbarger et al., 2007; Noske et al., 2008; Anderson et al., 2011; Saalfeld et al., 2012 ; Bock et al., 2011; Doroquez et al., 2014; Lee et al., 2016). Unfortunately, these procedures require a high level of training and are both time-consuming and prone to occasional loss of sections, that is, loss of information. Recently developed alternative methods for serial sectioning such as Serial Block Face – SEM (SBFSEM) and Focused Ion Beam – SEM (FIB-SEM), that use back-scattered electrons to image the block surface, have helped to address biological questions that require the analysis of large EM volumes (Denk and Horstmann, 2004; Heymann et al., 2006; Knott et al., 2011; Kizilyaprak et al., 2014; Titze and Genoud, 2016). During these approaches, the block surface is imaged, and then sections are removed. The new block surface is then imaged again. This cyclical repetition results in the generation of an automatically aligned stack of numerous sections. Although these approaches result in efficient 3D data acquisition, re-imaging the same sample at another region of interest or at a different resolution is impossible, as is on-section immunolabeling or post-staining contrast enhancement with heavy metals. These problems can be overcome, as has been shown in several studies that correlated light and FIB-SEM data on cells in culture, in brain tissue, and developing blood vessels in zebrafish (Bushby et al., 2012; Lucas et al., 2012; Maco et al., 2013; Lucas et al., 2014; Bosch et al., 2015; Blazquez-Llorca et al., 2015). Notably, such

elegant studies require rare and expensive equipment, available only in specialized labs with limited external access.

Array Tomography was developed by Micheva and collaborators to study protein localization in synapses (Micheva and Smith, 2007; Micheva et al., 2010; Collman et al., 2015). The samples are embedded in a hydrophilic resin and sectioned into long ribbons of serial sections (the arrays) using an ultramicrotome. The sections are then transferred to a glass coverslip (instead of a microscope grid) and analyzed by light microscopy followed by SEM. To localize a large number of proteins in a single series of sections, several rounds of fluorescence labeling were performed, using antibodies combined with an antibody elution step before each additional round. The EM-like sample preparation procedure enabled the analysis of the cellular ultrastructure with the localization of fluorescent signal.

Array Tomography (AT) is used in different procedures, depending on the research goal:

a. Multiplex FLM is used to detect numerous fluorophores (Table 1, Multiplex labeling). The mild sample treatment and hydrophilic resin embedding usually compromises the quality of the ultrastructure.

b. Serial EM is used for volume acquisition and Region Of Interest (ROI) recognition, when ultrastructural preservation is critical (Table 1, Volume reconstruction). Since the back-scattered SEM mode is used, high contrast with multiple heavy metal stains is required. This preparation uses standard or enhanced contrast TEM with epoxy resin based embedding.

c. Correlative Fluorescence-EM is used to preserve fluorescence and ultrastructure quality, both *en bloc* and on section (Table 1, CLEM). Freeze-substitution with acrylic resin embedding can provide efficient fluorescence retention (Nixon et al., 2009; Kukulski et al., 2011; Watanabe et al., 2011; Peddie et al., 2014; McDonald, 2014; Burette et al., 2015; Kremer et al., 2015; Paez-Segala et al., 2015; this study). However, the retention of the fluorescence signal with this approach is unpredictable and largely dependent on the specific fluorescent fusion protein used.

Although array tomography is a powerful technique, its use has been predominantly restricted to addressing questions in neurobiology, for which it was developed (Oberti et al., 2011). Recent studies have applied AT to other fields (Jahn et al., 2016; Markert et al., 2016). For AT, sections are cut and transferred to a solid support, such as a coverslip, an indium-tin oxide-coated coverslip, a silicon wafer or a Kapton plastic tape (Micheva and Smith, 2007; Pluk et al., 2009; Kasthuri et al., 2015) using special slide/wafer retraction mechanisms

(Wacker and Schroeder, 2013; Hayworth et al., 2014). AT-SEM is increasingly used as an alternative to TEM serial section SBF and FIB-SEM imaging methods to analyze large surface areas in a non-destructive manner. It allows the direct 3D correlation of CLEM samples with both fluorescence and electron microscopy data. Unlike other volume sections transferred to a solid support, these samples can be stored, re-imaged multiple times, and even re-contrasted with heavy metals to improve the signal-to-noise ratio (Schwarz and Humbel, 2014).

Large volume data analysis is required to answer some biological questions. Other questions can be answered by analyzing limited volumes from numerous independent samples or events. To provide a method to answer these questions that is accessible to the larger scientific community without technical limitations, we have modified and adapted the AT technique. Our method encompasses the entire procedure from sample preparation to data analysis. We transfer serial sections to glass coverslips or silicon wafers (hereafter referred to as 'wafer' for simplicity), label with heavy metals, and use high-resolution volume FLM and EM. We have optimized sample preparation, configured a diamond knife to facilitate the transfer of sections to support, and devised an efficient sectional screening strategy. This method can be used with a variety of model organisms. It does not require additional expensive equipment beyond that of most modern research facilities. To demonstrate our technique, we analyzed both *Caenorhabditis elegans* and *Drosophila melanogaster*.

Results

Sample preparation methods and sectioning strategy

When analyzing polarized samples and small model organisms, the relevant cellular structure, or region of interest (ROI), can be located using the known morphology and anatomy of the tissue as landmarks. The principal problem with these complex samples is that only one ROI may be present in each sample. Since imaging only one individual structure would be insufficient to make a statistically significant observation, numerous samples must be analyzed.

Our strategy to efficiently localize the ROI in a single sample includes two-step flat embedding, precise block trimming (Figs 1A, B; Kolotuev, 2014), and serial sectioning. We use light microscopy to rapidly locate the ROI for subsequent EM analysis, precisely orient the sample, and delimit the area for ultrathin sectioning. To optimize the stability of the

ribbon of consecutive sections, we remove the excess embedding resin surrounding the sample. With homogeneous tissue, excess embedding resin can be easily trimmed away from a sample (we refer to this as "tight trimming"). With non-homogeneous tissue, such as *C. elegans* or *Drosophila,* even "tight trimming" cannot entirely remove the excess resin. Thus, we use our trimming diamond tool for "tight trimming" to leave a minimal amount of excess resin around the sample. To acquire long ribbons of consecutive sections (>300 sections), we prefer to shape the surface of the block to a rectangle, with the edge parallel to the knife, such that the block length measures twice the length of the side edges. A larger sectional surface tends to produce more folds, while sections with a smaller surface tend to curl.

To produce horizontally aligned sections on support (glass coverslips or wafers), we used a modified diamond knife that greatly facilitates the efficient generation of long ribbons of consecutive sections (Figs. 1C-H; see detailed description below). Left intact, these long ribbons can complicate subsequent manual data acquisition: Without obvious structural variation, mistakes will often be made during the monotonous analysis of long ribbons of consecutive sections. Thus, for our rapid screening approach, we carefully subdivide the long ribbons initially produced into shorter ribbons of consecutive sections (50-100 sections), and then horizontally align the shorter ribbons alongside each other, side by side, in rows on the support. This way, 10 short ribbons (*i.e.*, over 500 sections) can be easily aligned on a small support, be it a coverslip, or a wafer (Fig. 1H). Then, instead of thoroughly analyzing every section within a long ribbon in a serial "vertical" fashion (from 0 to 100+), we "leap" between centrally-located sections across the short horizontally-aligned ribbons to visually screen for the ROI (see detailed example below).

Sequential section analysis using TEM grids is very tedious: Numerous problems can emerge. If the sectional surface is relatively large, then very few sections will fit on one grid. If multiple sections do fit on one grid, then sample collection is error-prone due to the risk of sectional loss. Data analysis is also very time consuming because each section on the grid must be manually screened to find the ROI and orient the sample. For serial section collection, even a relatively short sequence of sections (e.g. 100) transferred to support (glass coverslips or wafers) presents significant advantages compared to sections on TEM grids (Figs. 1I, 1J). On support, 115 serial sections can be analyzed in less than 15 minutes after orienting the trimmed block optimally relative to the AT knife. To analyze 115 sections on TEM grids would require much more time and result in significantly less precise data. For any

scientific question that needs a resolution compatible with FIB and SBF-SEM, our transfer technique has clear benefits over serial section TEM.

Modified diamond knife

Both the histo and the ultra-Jumbo knives (Diatome, Switzerland) hold a coverslip in their large boat at an optimal angle for collecting semi-thin sections. These knives can be used to generate arrays of sections, that is, long ribbons of consecutive sections. In the published AT procedure, the array of sections is moved to the rear edge of the coverslip where it touches the interface between the glass and the water (Micheva and Smith, 2007). To attach the sections to support, water is drained from the side of the knife boat using a syringe (Micheva and Smith, 2007) or the coverslip is pulled out of the trough using a micromanipulator (Horstmann et al., 2012; Wacker et al., 2016). In our hands, this method compromises the control of water during draining. The resulting rapid drying of the sections on support can create wrinkles or folds in the sections and cause ROIs to be lost from view.

We have developed a water-draining system for the histo jumbo diamond knife, which reduces the incidence of sectional folding and wrinkling. Also, we have replaced the blade on the diamond knife and increased the size of the knife boat to better suit AT:

1. We replaced the diamond blade for the histo jumbo diamond knife for semi-thin sectioning (~500 nm) by the diamond blade for the ultra 35° knife for cutting ultrathin sections (~50 nm). Ultrathin sections have better quality than semi-thin sections: Unlike semi-thin sections, ultrathin AT sections with a thickness of 50-100 nm give better z-resolution and generate fewer folds. Ultrathin sections also improve the quality of subsequent analysis, as they adhere better to the support and provide higher ultrastructural resolution.

2. We increased the size of the knife boat to completely accommodate a coverslip on a flat support on the bottom of the trough at a 0° angle. The support for the coverslip is surrounded with a ditch to allow for user-controlled water draining. A hole in the bottom of the boat facilitates the insertion of a flexible tube attached to a syringe (Figs. 1C, D). Using the syringe, water can be added to or retracted from the boat without creating turbulence, which had presented problems while using previous methods (Fig. 1E). To attach the sections to support, water is drained slowly through the hole in the bottom of the boat. Slow water removal avoids turbulence and allows the sections to dry slowly, without wrinkles and folds.

This technique of attaching the section ribbons to support is the same for all types of support: After generating the ribbon of the desired length (Fig. 1F), the water level in the boat is gradually lowered, by draining the water slowly through the hole in the bottom of the boat, either actively by aspiration with the syringe or passively, by allowing the water to drip through the tube without a syringe attached to it (Fig. 1G). When the water level reaches the height of the transfer support, the sections are manually aligned and arranged side by side (Figs. 1G, H, Movie 1). In our experience, this method greatly facilitates the ease and accuracy of section transfer for CLEM and volume EM. The same principle can also be used to collect histological sections for light microscopy analysis.

Multiplex immunolabeling

The immunolocalization of antigens is compromised by low Z-resolution for both standard and super-resolution light microscopy. Also, the co-localization of multiple antigens using antibodies generated in the same species is often problematic. The advantage of AT is that sections can be cut as thin as 40 nm, and images of several cycles of immunofluorescence labeling can be acquired individually and then superimposed. Physical ultra-thin sectioning can achieve a Z-resolution of a few tens of nanometers, which is an order of magnitude better than the Z-resolution of currently available super-resolution microscopes.

C. elegans is a transparent worm, which makes it an ideal model organism for light microscopy. Unfortunately, most specific primary antibodies available for *C. elegans* research are restricted to either mouse monoclonal or rabbit polyclonal. Thus, the co-localization of multiple antibodies on the same sections is often impossible. To demonstrate the power of the AT approach, we labeled serial sections of *C. elegans* larvae prepared by high pressure freezing (HPF-FS; see the Materials and Methods sample preparation section for details) on coverslip support. We stained/labeled the arrays of 100 nm thick sections with DAPI (nuclei, blue), anti-tubulin (red), and anti-*erm-1* (EB1, green) in the first cycle and, after destaining, we stained for DAPI, anti-actin (red), and anti-*vha-5* (green) in the second cycle (Figs 2A, B). Both rounds of immunolabeling gave a strong signal, equally visible on individual sections and on the merge of all 25 sections (Figs 2A, B, Movie 2). Before relabeling and reanalyzing the samples, we extensively washed the sections between the labeling cycles, and verified that the previous labeling had been completely removed. We used the manual acquisition of the images, improved their alignment by developing a new Fiji macro, and superimposed all markers in one data set (Fig. 2C). DAPI nuclear staining served as a useful reference marker

to facilitate the alignment of the complementary signals provided by the two independent labeling cycles.

To monitor the quality and feasibility of EM acquisition, and to correlate the labeling data on sections after two labeling cycles, we imaged the corresponding ROIs with the SEM using the back-scattered electron (BSE) detector. The fluorescence signal could be identified quickly, and the overall ultrastructure was well preserved (Fig. 2D). To improve the accuracy of superposition, we used DAPI nuclear staining and examined the nuclear ultrastructure and other structural features of the sample (Fig. 2E).

Localization of ROI and volume reconstruction

In complex tissues, drawing conclusions about the ultrastructure from a single section or a small number of sections can be impossible. Volume reconstruction of cells and tissues using the SBF and FIB-SEM methods is an efficient way to investigate the relationship between cells and organelles in their complex 3D cellular context. For both approaches, however, the ability to precisely target the ROI remains challenging and requires endogenous landmarks (Karreman et al., 2016). To illustrate the advantages of an AT-based solution in targeting the ROI, we imaged the *Drosophila* ovarian chamber at stage 3. Our previous efforts with the ovarian chamber had already exposed us to the difficulties of localizing the ROI in this tissue, and had actually prompted us to develop our current AT method that enables more direct sampling and screening.

Drosophila oogenesis is often used to model cellular processes, such as cell division, cell migration, and stem cell differentiation (Horne-Badovinac and Bilder, 2005; Fuller and Spradling, 2007; McLaughlin and Bratu, 2015). During development of the ovarian chambers, the exterior follicular cells, the internal nurse cells, and the oocyte undergo numerous structural changes. Nurse cells, which supply the necessary nutrients and cell building material to the oocyte, do not accomplish abscission but remain interconnected through the network of ring canals. During development and cell growth, the initially small ring canals expand in diameter by about ten-fold (Robinson et al., 1994; Hudson and Cooley, 2010; McLean and Cooley, 2013; Hudson et al., 2015). Imaging the ring canals (RCs) in their entirety using EM is difficult, mainly due to their large size and random distribution inside the ovarian chamber. On single sections, the RCs frequently appear as two spaced bars or brackets, and not as a circular structure, as in FLM micrographs. Based on our experience,

localizing the RCs with FIB-SEM or SBF-SEM tomography is problematic (Loyer et al., 2015).

We prepared the ovarian chambers using chemical fixation and flat embedding, sectioned, and then transferred the ribbons of sections to wafers. Our fast screening strategy rapidly localized the RCs within the arrays of sections at low magnification. Then, we assessed the general orientation of the organism in a flat embedded sample based on the anatomy of the sample (Fig. 3A). After sectioning, we localized the RCs based on known landmarks in the organism. For this, screening the sections on wafer at low magnification resulted in the rapid identification of regions to analyze at higher resolution (Figs 3B, C). Initially, we collected ribbons of consecutive sections, aligned them side by side, and then tracked cellular features (or landmarks) along these ribbons (In Fig. 3B, each ribbon of sections is colored distinctly). For faster screening, the sections were not screened in consecutive order but rather "horizontally," by scanning the middle section from each ribbon for RCs (Fig. 3C; the color of the frame corresponds to the color of a given portion of the array, selected in proximity to the white arrow at the panel B). Once a RC was recognized and located (Fig. 3C, orange), we could easily track the entire relevant sequence of sections by sequentially following the sections along the ribbon, using the reference section as an anchor. This simplifies the screening logic: One starts from the beginning of the relevant sample portion and then collects sections for as long as necessary. In this way, the localization of anatomical features is more efficient, rapid and precise, avoiding the acquisition of unnecessary data sets.

To localize the four ring canals that connect the future ovary and the nurse cells, we applied the above-described screening strategy. At low magnification, we identified ring canals in sections and as expected, the canals appeared only partially and did not resemble rings (Fig. 3D). After acquisition, the overlay of the sections allowed the modeling of the rings in their entirety, as well as the identification of the position of the ring on the cell surface (Movie 3). The same set of sections can be reused to reconstruct the interaction between additional pairs of cells in the same ovariole, or the sections can be reimaged to analyze the structure of the RC in ovarioles of another developmental stage. Since the sections remain intact on the surface of the wafer, a ring of particular interest can be revisited using different acquisition parameters for more detailed study (Fig. 3E, Movie 4). The aligned data set can be further analyzed using different modeling and rendering programs, providing the precise identity of different cells, their spatial distribution, and interactions (Figs 3F, G, Movie 5). The resulting data can be further mined by targeted analysis of relevant 3D data portions (Fig. 3H, Movie

5). Once the various stages of ovarian chambers and ring canal maturation have been collected and maintained on wafers, a library can be established. As in the case of ovarian chambers, any sample collected on wafers can be reanalyzed and reimaged when new questions arise. Arrays can be stored indefinitely and, with proper annotation, can be used by several different research groups. In addition to the examples presented here, this strategy can be applied to answer similar questions in other complex tissues (Fig. S1).

Correlative labeling of samples on wafers: fluorescence retention

We next extended our multiplex immunolabeling protocol and 3D screening with a reconstruction strategy, focusing on an organism bearing genetically encoded fluorescent markers. To retain the endogenous fluorescence *en-bloc* for AT, we tested several preparation protocols. Using high-pressure cryofixation and quick freeze substitution in acetone-containing uranyl acetate with subsequent embedding in HM20 methacrylate resin gave the most satisfactory results. With this, we could visualize various fluorescent constructs, both *en-bloc* and on section (Figs 4A-D), facilitating the localization of the ROIs in 3D. Moreover, searching for the fluorescence signal in a light microscope helped to localize the ROI faster, than does EM screening for desired morphological features. We processed *C. elegans* larvae using this protocol. In addition to the endogenous signal, the sections could be labeled with antibodies, providing additional data (Fig. 4C). Here again, the superposition of the fluorescent and the EM images was reliable and straightforward, making the direct CLEM reconstruction and analysis precise and unambiguous (Fig. 4D).

To further facilitate rapid correlation of ROIs and automate the acquisition process, we used the FEI 'MAPS' software. This provided automatic acquisition of both fluorescent and SEM images. We then superimposed these images, allowing the transfer of the same "geographical" parameters from one type of microscope to another (Loussert Fonta and Humbel, 2015). Using the FEI CorrSight light microscope and MAPS software, large regions can be acquired automatically at low magnification (x10) with the separate single images stitched together to form one large file. This provides an overview of the sections on the support that is useful to identify the current location within the ribbons of consecutive sections. Imaging is then done using various objectives, imaging modes, and several fluorescence channels to localize the proteins of interest. For correlation, high-magnification (x63, x100), large-scale images of the fluorescent structures on the relevant sections can be acquired by tiling (Fig. 5A). After light microscopy, the project, containing the recorded light micrographs can be transferred to a (FEI) scanning electron microscope (Fig. 5B). Using

anatomical landmarks, all light micrographs can be aligned and overlaid on the map of the electron micrograph and high-resolution electron micrographs can be recorded (Schwarz and Humbel, 2014).

To highlight the versatility of this technique, we analyzed the excretory canal of *C. elegans*. This single cell organ is located in the pharyngeal region of the worm and, during development, sprouts four tubular extensions that run the length of the entire body of the animal (Fig. 5C; Kolotuev et al., 2010; Kolotuev et al., 2013; Sundaram and Buechner, 2016). Fast HPF-FS preparation enabled the preservation of the fluorescent *vha-1::GFP* signal (Fig. 5D). This greatly facilitated the recognition of the ROI after transfer to SEM, as the image has a similar appearance in both modalities.

The MAPs program can facilitate the automatic acquisition of both fluorescence and SEM images, subsequently superimpose these images, and provide a result analogous to that of the "Google Earth" principle: First, images are acquired using low magnification (Fig 5B) and then higher magnification is used (Figs 5E, F). Finally, "stitched images" are composed of several single images at a given resolution so that both the overall field of view and the individual images of particular ROIs can be reused for future analysis. Compared to analyzing sections on TEM grids, using arrays permits the analysis of larger sections. Thus, more individual samples can be simultaneously collected (Fig. 5E, n>30, yellow). The fluorescent signal is easily detected on sections, facilitating identification of animals in the desired orientation and/or developmental stage. After the appropriately oriented sample is identified via FLM, SEM using manual correlation, based on either the position of the sections; alternatively, a MAPS-mediated site localization can easily detect it. After the ROI has been found on a reference section, one can select the desired resolution for the EM acquisition (Figs 5G, H). Then the necessary ultrastructural data can be obtained by volume reconstruction (Fig. 5I). Within the tissue, the desired cell type can be ultrastructurally indistinguishable and/or difficult to localize. One example is the cell body of the early larval stage excretory canal, which is located in a densely packed environment and is not evident on routine ultra-thin sections. The fluorescence signal can aid in identifying a particular cell at the ultrastructural level (Fig. 5G). Once the fluorescence signal allows recognition of the cell of interest, EM analysis of the subsequent sections no longer requires correlation with the fluorescent data: The position of the cell on subsequent sections becomes evident (Fig. 5H).

The adult excretory canal extension is 100-1000 μm long and 50-100 nm in diameter, making it difficult to image the overall volume of the canal arms using SEM. Only very rarely does

the fixed animal remain straight after processing, so orienting for longitudinal sectioning is a tedious procedure. Usually, only a small portion of the body can be correctly oriented. Locating an ROI may require screening and acquisition of hundreds of carefully collected serial sections (Fig. 6A). Thus, it is complicated to precisely orient these extensions for longitudinal sectioning. The specimen often curves after fixation, and the recognition of the defragmented structure without the overall body context is often difficult, as the same structure appears differently and in a different location depending on the sectioning axis (Fig. 6B). In this case, the fluorescence served as a landmark to permit the easy recognition of the cells of interest. For this purpose, we labeled the excretory cell in green, and a random cell in its vicinity in blue. Superficially, these cells appeared identical, and if one had to distinguish them by a 'blind search', it might be impossible.

Here again, the combination of fluorescence-mediated screening with subsequent targeted EM acquisition facilitates precise orientation. First, the appropriate fluorescent image is found on section. It is useful to label the sections with the nuclear marker (DAPI, Draq5) to assess the orientation of the sample and to avoid confusion in repositioning the fluorescent signal on the EM data. Second, fluorescence data rapidly guides the analysis to the relevant ROI, after which the required number of sections or the desired volume of data is collected (Fig. 6C). In our example, the sections are spaced less than 200 nm apart, and the portion of the canal that connects the extension to the cell body is no longer seen from one section to another (Fig. 6D, arrow). Without fluorescence, the detached part would not have been evident for the recognition using only the EM data only (Fig. 6, arrows).

Our results demonstrate that when the endogenous fluorescence signal is preserved throughout the preparation, the random-sectioning approach facilitates identification of randomly-oriented samples. When combined with the MAPS correlation software, the structures of interest can be rapidly identified and imaged at high-resolution by EM, enabling fast-throughput analysis of a statistically significant number of organisms.

Discussion

This study presents an efficient array tomography (AT) procedure to facilitate the analysis of a single region of interest (ROI) in a whole organism on serial sections that is applicable for numerous biological samples. On serial sections, the ROI can be labeled with a fluorescent tag and correlated with the corresponding electron micrograph. The serial sections can then be quickly screened using fluorescence or directly SEM.

Besides the SEM, our method does not require additional expensive equipment for an EM lab or facility. The newly designed diamond knife we introduce can be used with any ultra-microtome, and its application is technically easier than performing classical ultrathin sectioning. In contrast, the approach using serial-block-face with focused-ion-beam scanning microscopy has a very high cost and limited accessibility. An alternative approach using the ATUMtome machine for automatic section collection from neuronal samples was recently demonstrated (Kasthuri et al., 2015). Likewise, an alternative AutoCUTS method was recently used to collect sections of *C. elegans* larvae (Li et al., 2017). However, this time-consuming and more expensive strategy is only worthwhile when there is a requirement for thousands of sections, as is often needed for brain samples. In contrast, our direct AT method requires a modified diamond knife, while the ATUMtome strategy requires an expensive and specialized machine (available at selected facilities only).

For both the ATUMtome and our direct AT method, libraries of serial sections can be stored indefinitely and reanalyzed to address future research questions. For studies involving multiple organisms or organs, for which neither serial section TEM nor volume EM approaches would be efficient, our screening method provides an accessible solution. For questions that can best be answered by analyzing many different samples (e.g., wild-type vs. mutants), libraries of AT sections can be extremely useful. A single 2 x 4 cm wafer can contain all the necessary information to permit the analysis of a small organism quickly. Also, the researcher needs not to immediately acquire the entire sectional area at high resolution, as is done with block-face microscopy. High-resolution collection of only relevant data results in greater precision and shorter acquisition time. Less electronic data are stored, as information that is irrelevant to the initial question are not collected. Thus, statistically significant EM volume data can be acquired in a timely fashion. Further, compared to block-face methods, the sections generated by AT can first be imaged at low magnification for orientation, and

then the ROI can be imaged at higher resolution for a more detailed analysis. Direct CLEM, with or without automation, can provide an additional level of volume correlation and can simplify the EM identification of similar structures. The fields of cell and developmental biology, model organism analysis, and even clinical research could benefit from this technique to address such mechanisms as cell migration, tissue remodeling, and the fine structure of cell division and abscission (Fig. S1).

Most of the technical problems with the use of the existing SEM imaging fields and modalities relate to the lack of precision of automatic acquisition. Current software systems that support array tomography include Atlas, with Zeiss scanning electron microscopes, and MAPS, with FEI electron microscopes. With both software systems still in development, future improvements could facilitate the automation of robust and efficient serial section acquisition: For example, the acquisition process could be automated, and more solid and user-friendly data alignment algorithms could be provided.

In conclusion, our AT method can be used to resolve long-standing questions in cell and tissue biology that require 3D ultrastructural analysis, and to localize antigens in defined structures. This approach could be useful for both biological research and clinical analysis, as high-quality results can be efficiently achieved using equipment that is, to a large extent, already present in many imaging facilities.

Materials and methods

Sample fixation and processing

The samples were either chemically fixed or processed using the high-pressure freezing – quick freeze-substitution method (Table 1).

Chemical fixation: The samples were fixed for 2h at ambient temperature in 2% (w/v) formaldehyde and 2.5% (w/v) glutaraldehyde dissolved in 0.1 M phosphate buffer, pH7.4 (EMS, 19340-72, 11650, 19344-10 respectively). They were then post-fixed in 1% (w/v) osmium tetroxide (EMS, 19152) and 1.5% (w/v) potassium ferricyanide in cacodylate buffer (EMS-26604 1A) for 1h at ambient temperature, followed by 1h incubation in 1% (w/v) tannic acid (Sigma-Aldrich, #403040). After extensive washes in water, the samples were incubated in 2% osmium tetroxide followed by 1h in 1% (w/v) uranyl acetate in water and dehydrated in an ascending series of ethanol followed by an ascending concentration of

EPON (EMS, 1420) in ethanol mixtures (Starborg et al., 2013; Kolotuev, 2014). Finally, the samples were flat embedded using a two-step procedure, and then polymerized at 60°C for 48h as previously described (Fig. 1A, Table 1; Kolotuev, 2014).

Cryo fixation quick freeze-substitution was performed using a modified version of the previously described method (McDonald, 2014). Carriers containing HPF immobilized samples were transferred to vials containing freeze substitution media (0.1% (w/v) uranyl acetate, 2% (v/v) H_2O in acetone) and then placed in the freeze-substitution unit (AFS2; Leica Microsystems, Vienna), cooled to -140°C, and heated to -50°C over 8h. The samples were then infiltrated by ethanol and resin mixtures. After freeze-substitution, the samples were flat-embedded, either in EPON embed 812 resin (EMS, 1420 morphology analysis), or in the monostep HM20 hydrophobic methacrylate resin (EMS, ref 14340) for the samples containing fluorescently-tagged proteins, or those to be used for immunofluorescent labeling (Table 1; Kolotuev, 2014).

Block preparation and serial sectioning

Blocks were trimmed to ∼100×200 µm cuboids using a trim 90-diamond blade (Diatome). Sample block sides parallel to the knife were coated with a mixture of one part Weldwood contact cement (SADER® NÉOPRÈNE LIQUIDE) to three parts xylene. This mixture increased the adhesiveness of the sections to each other to produce a long ribbon of consecutive sections (>300). The resulting long ribbons of consecutive sections were subdivided into shorter ribbons (50-100 sections) and then aligned on support, side by side (Kolotuev, 2014).

To generate planar arrays of sections on support, we used a modified ultra 35º diamond knife with a custom-built boat (Figs 1C, D; Diatome, Switzerland; see Results for details) mounted on a Leica UC7 ultramicrotome (Fig. 1E; Leica Microsystems; Vienna, Austria). Ribbons of consecutive sections were generated with a length that varied according to the eventual goal of the AT procedure: 50-200 sections per ribbon, 50-150 nm thick. Each array of ribbons aimed for multi-labeling was transferred to a glass coverslip (VWR ref 631-1575), or, if it was dedicated for EM reconstructions and CLEM, to a silicon wafer (Ted Pella, No 16015). Before use, glass coverslips were cleaned and coated with 0.5 % gelatin solution (EMS 16564) added to 0.05 % chromium potassium sulfate (Sigma-Aldrich, ref 243361), following a previously described procedure (Micheva et al., 2010). We followed the manufacturer's

instructions to obtain a 1-2 nm carbon layer for the samples collected on the glass slide using CCU-0101 LV machine (Safematic GmbH, Switzerland). A thicker layer can compromise the quality of the SEM images. Image collection on the ITO coated slides should eliminate the need in this step (unpublished observation, IK, AM).

Round wafers were cut into 2x4 cm rectangles using glass breaking pliers 6'' (Ted Pella, ref 7295), cleaned, and glow discharged for 30 seconds using the current plasma HT of 15mA (Cressington 208, Cressington Scientific Instruments Ltd, UK). We did not carbon coat the samples on wafers since we did not detect any charging effect during the image acquisition.

Improving quality of arrays on sections: avoiding folds

Sectioning problems can compromise both the quality of the sample and the reliability of the subsequent analysis. The appearance of wrinkles on the surface of sections can ruin the entire AT data set. The impact of a fold on data analysis is difficult to quantify, mainly because only folds that affect the ROI are deleterious.

We distinguish two types of wrinkles that can appear on the surface of sections: (a) folds, causing global damage to the section, and (b) micro-folds, small wrinkles in limited areas of the sample surface. We could detect both types of wrinkles on sections, but frequently they affected only the excess embedding resin surrounding the sample. Also, on several sections, the wrinkles could be found on the sample surface, without affecting the ROI (Figure S2). Even in very extreme cases of severe wrinkles, it is difficult to interpret their impact on data analysis. In Figure S3, four independent samples of a section are shown. Even if the samples No. 1, 2, or 3 have large folds or debris, this will not affect the data analysis. However, if the sample No. 4 had a fold in the bottom half, it would only be ruined if we were interested in its bottom half. If we wanted to analyze its upper half, then the wrinkle would not affect our analysis. The situation with micro folds is very similar if they happen to occur within the sample but not within the ROI (Figure S3). Thus, we decided not to quantify the number of folds but rather to characterize the conditions under which they appear and possible ways to prevent them.

Below we list factors that can lead to folds and wrinkles and how these can be minimised.

Block surface size and section homogeneity

The size of the sample surface appears to be essential: Smaller sections result in fewer wrinkles because there is less surface to generate wrinkles. Further, density differences between the sample can influence the quality of sectioning. Epoxy resin will create a co-polymer within the biological sample, which has a different density than the empty resin. Thus, excess embedding resin should be removed. Within homogeneous tissue, all excess resin is removed, leaving only a rectangular block of embedded tissue. For smaller non-homogeneous samples such as *C. elegans* or *Drosophila*, it is difficult or impossible to remove the entire resin around the sample. Thus, we advise maintaining a similar amount of resin on each side of the sample.

For better stability of the ribbon of consecutive sections, it is important to trim the block as close to the sample as possible, shaping its surface into a rectangle, with the edge touching the knife measuring twice the width of the side edges at the side. A larger section surface produces more folds, while sections with a smaller surface tend to curve more. Curving of the ribbon of consecutive sections that is, section curling, is problematic, especially for ribbons that will be aligned side by side on support. With some experience, this problem can be overcome (Movie 1).

Section thickness

This parameter is as important as the block edge size and has a significant effect on the quality of the resulting sections. Ultra-thin (50-80 nm) sections attach better to the support and have fewer micro-folds compared to semi-thin sections (100-250 nm).

The speed of water retraction during section drying

We found the rate of water retraction to be critical for successful transfer of the ribbons of consecutive sections to the slide support. The support surface should be hydrophilic. Excessive hydrophobicity of the support can cause folds in the sections. Thus, supports dedicated for SEM analysis (wafers, glass slides, or Kapton tape) should be carefully pretreated using a standard glow discharge procedure. Even with a very disorganized collection of sections, if the process of drying was optimal, there is a lower chance of the appearance of folds (Figure S4, can be zoomed in) and the development of microfolds in non-homogeneous samples is much less likely to occur.

Occasional debris on the section surface can be difficult to eliminate. To reduce the occurrence of debris, the knife and the basin must be meticulously rinsed with distilled water

filtered with a 0.22 µm syringe filter. Coated glass slides must be carefully prepared, and wafers, thoroughly cleaned. Water filtering and knife cleaning before the generation of the sections can help to minimize the accumulation of dust and debris on the surface of the sections.

Sample treatment for FLM, EM, and CLEM

Multiplex fluorescent labeling: Labeling the arrays with a subset of different antibodies was carried out using a previously described procedure (Micheva et al., 2010). Briefly, ribbons of consecutive sections on a glass coverslip were incubated in a humidity chamber with 50 mM glycine solution in TBS (Sigma-Aldrich, T5030) for 5 min., then with blocking solution containing 0.1 % BSAc (Aurion, 900-099) in TBS for 5 min. Specific primary antibodies mouse anti-actin (Cedarlane CLT 9001), mouse anti-tubulin (Invitrogen 322500), rabbit anti VHA5 (courtesy of Dr. Labouesse) and rabbit anti EB1 (Santa Cruz SC 15347) were diluted to 1:100 v/v in TBS and incubated overnight at 4°C (Nicolle et al., 2015). Secondary antibodies Cy2 anti-mouse, (Abcam Ab-6944) and Cy3 anti-rabbit, (Abcam Ab-6939) were diluted to 1:100 v/v in TBS and incubated at ambient temperature for 2h.

Samples were mounted using the *VECTASHIELD* ® Antifade Mounting Medium (Vector Laboratories, H1200) and imaged the same day. DE staining and relabeling of the arrays was done according to the experimental requirements (Micheva and Smith, 2007). For removing the bound antibody complex, a mixture of 0.2 M NaOH with 0.02 % SDS was applied to the samples for 20 min. followed by extensive washing cycles. Before relabeling using the same method as the initial labeling, the samples were dried in an oven at 60ºC for 20 min.

After completion of fluorescent image acquisition, the samples were extensively washed in double distilled water, dried and contrasted for 15 min. in a 4% uranyl acetate solution followed by a 10 min. incubation in Reynolds lead citrate solution.

For SEM acquisition, samples prepared using the high-contrast procedure were directly observed without further manipulation. For all other acquisitions, the sample contrast was increased using the same parameters as for CLEM experiments.

Fluorescence on sections

Multiple fluorophores and fluorescence preservation procedures for CLEM have been developed (Nixon et al., 2009; Kukulski et al., 2011; Watanabe et al., 2011; Peddie et al., 2014; McDonald, 2014; Burette et al., 2015; Johnson et al., 2015 ; Kopek et al., 2017). Though efficient for many types of proteins, the level of fluorescence of genetically encoded markers on sections varies from construct to construct. Although we did our best, we could not predict under which preparation conditions it would be preserved at all, and to what extent. For some constructs, fluorescence remains visible inside the block and on sections even without using an anti-bleaching solution. For other samples, even if we were not able to detect signal inside the block the fluorescence was often visible in the sections. For these samples, we could preserve the fluorescence signal for at least one year after the preparation. For some samples, however, although the fluorescence signal was initially present, we were not able to preserve the fluorescence in blocks or on section. A systematic analysis of fluorescence preservation as a function of a protein type (transmembrane, cytosolic, secretory, etc.) could further facilitate our understanding of the problem of fluorescence preservation. In the future, we hope to combine our observations with those of other groups that have experience with fluorescence retention using other species and fluorescent constructs to understand the factors influencing the fluorescence retention and to develop a robust preparation protocol.

Intuitively, thicker sections should provide a better fluorescence signal when genetically encoded markers are used. However, there is a thickness-to-stickiness relation, in addition to the loss of EM details in thicker sections: Thinner sections had better adherence to the surface. Also, photo-bleaching was even more troubling. Thus, to find a reliable way to quantify the "signal emission" from sections of different thickness might require complicated math/physics calculations, which would likely not be applicable for all types of fluorescent constructs. However, the overall preservation of sectional fluorescence is a concern because, after fixation, the signal is not linear and varies with the type of construct.

Image acquisition

Fluorescent microscopy acquisition and image treatment

Wide-field fluorescent image acquisition was made using a Leica DMIRB inverted microscope or a Leica DMRXA upright microscope equipped with a 20x/0.4 NA plan, a 63x/0.7 NA PL Fluotar or 100x/0.7 air and 1.4 NA PL APO oil objectives, and a Coolsnap HQ2 CCD camera (Photometrics, Tucson, USA).

Confocal fluorescent images were taken using a Leica TCS SP8-SMD confocal microscope equipped with both 63x/1.4 NA Oil HC PL APO and 40x/1.3 NA Oil HC PL APO objectives (Leica Microsystems, Mannheim, Germany). Fluorescence signals were collected sequentially through Leica photon-counting hybrid detectors to increase the signal-to-noise ratio.

For light microscopy tile acquisitions, the CorrSight light microscope (FEI Company Munich, former Till Photonics) running the MAPS software (Thermo Fischer, former FEI Company, Eindhoven) was used (Loussert Fonta and Humbel, 2015). The microscope is equipped with Zeiss objectives (Zeiss, Munich): 5x NA 0.15, 20x NA 0.8, 40x NA 0.9 and 40x NA 1.3 oil immersion; and DAPI, 488 nm, and mCherry filters. The light micrographs, bright field, and fluorescence were recorded with MAPS and stored as an aligned package in a project.

For SEM acquisition, we used a JEM 7800F with retractable backscattered electron detector (JEOL, Japan), with the following parameters: Accelerating voltage: 8 kV, Probe current: 1.6 nA, WD: 5mm, dwell time: 10 µs/pix with 4096 x 4096 frame size. For MAPS-related experiments, FEI Quanta FEG 250 SEM (Eindhoven, Holland) was used with the following parameters: Accelerating voltage: 10 kV, Probe current: 0.8 nA, WD: 7mm, dwell time: 30 µs/pix with 4096 x 4096 frame size. The MAPS projects were transferred to the Helios 650 FIB-SEM (Thermo Fischer, former FEI Company, Eindhoven, Holland). A reference image was taken with SEM. Light micrographs were then aligned to this image and used to find the region of interest to be analyzed at high resolution using SEM (Loussert Fonta and Humbel, 2015).

Alignment and reconstruction

To align the fluorescent stacks of sections, we developed the computational volumetric analysis protocol, based on Fiji and ICY programs (Schindelin et al., 2012; de Chaumont et al., 2012). The co-registration procedure will depend on the data set. Using Fiji software, we selected *C. elegans* embryos in each stack using an automatic threshold, and signals located outside of the chosen area were deleted. The first two steps can be done automatically using a rigid registration. Indeed, as images come from the same array with a microscope always using the same settings, the displacements between two images are rotation and translation. In the image processing community, numerous algorithms aim to solve rigid registration task. We used the "Register Virtual Stack Slices" available on Fiji (http://imagej.net/Register_Virtual_Stack_Slices). This method uses the SIFT feature to find corresponding regions in images pairs. To facilitate the use of this registration algorithm for array data, we developed a Fiji macro that runs in three steps:

The co-registration procedure will depend on the data set.

(1)   "Split Stack": this step splits the array hyperstack into various image sequences, one sequence for each staining of the FLM data. The sequences are stored in output subfolders C1, C2 … The operator need only to specify the number of channels (i.e., staining) in the stack.

(2)   "Register Reference": this step calculates the registration transformation matrices using the reference staining. Usually, the DAPI staining is used as a reference for FLM. The operator needs only to provide the reference channel directory (C1 or C2 or …), and the output directory where the transformation matrices will be stored. This directory is already created by the macro, the operator can simply select it. The algorithm settings are (a) reference channel: channel used to estimate the transformation. (b) Registered image size: size of the output image canvas. It should be larger than the original image for all of the images that have been transformed to fit into the canvas.

(3)   "Apply transformation" This step applies the transformations calculated in (2), to all of the staining series (C1, C2, …)

Depending on the image content, the registration algorithm may fail to locate any corresponding regions between the separate array images. This can be resolved using pre-filtering of the reference staining before registration (i.e., between Step (1) and Step (2)). The operator can then apply a filter to enhance the brightness, the contrast, or the gradient of the array. This optional step had not been implemented in the macro since it is application dependent. The use

of the macro is similar to registering LM and EM array, but for the EM alignment, a single channel C1 is used.

EM / FLM registration: This registration cannot be done automatically since the resolution, and the content of images are different. Thus a supervised registration method is required. For this, landmarks that match the reference regions on FLM and EM micrographs are used with the ICY plugin ec-CLEM (Paul-Gilloteaux et al., 2017). We co-registered arrays obtained with the macro described above and registered the first image of the C1 FLM array and the first image of the EM array with ec-CLEM. A detailed tutorial of ec-CLEM is available at http://icy.bioimageanalysis.org/plugin/ec-CLEM. ec-CLEM generates a file containing the registration transformation matrix. The operator can then apply this transformation to all of the FLM arrays with ec-CLEM.

For the SEM data alignment and 3D modeling, we used IMOD, Fiji, and Photoshop software (Schindelin et al., 2012; Kremer et al., 1996). To achieve a TEM-like appearance, the SEM micrographs were contrast-inverted using IMOD or Adobe Photoshop.

References

Anderson, J. R., Jones, B. W., Watt, C. B., Shaw, M. V., Yang, J. H., Demill, D., Lauritzen, J. S., Lin, Y., Rapp, K. D., Mastronarde, D., et al. (2011). Exploring the retinal connectome. *Mol Vis* **17**, 355-379.

Blazquez-Llorca, L., Hummel, E., Zimmerman, H., Zou, C., Burgold, S., Rietdorf, J. and Herms, J. (2015). Correlation of two-photon in vivo imaging and FIB/SEM microscopy. *J Microsc* **259**, 129-136.

Bock, D. D., Lee, W. C., Kerlin, A. M., Andermann, M. L., Hood, G., Wetzel, A. W., Yurgenson, S., Soucy, E. R., Kim, H. S. and Reid, R. C. (2011). Network anatomy and in vivo physiology of visual cortical neurons. *Nature* **471**, 177-182.

Bosch, C., Martinez, A., Masachs, N., Teixeira, C. M., Fernaud, I., Ulloa, F., Perez-Martinez, E., Lois, C., Comella, J. X., DeFelipe, J., et al. (2015). FIB/SEM technology and high-throughput 3D reconstruction of dendritic spines and synapses in GFP-labeled adult-generated neurons. *Front Neuroanat* **9**, 60.

Bumbarger, D. J., Crum, J., Ellisman, M. H. and Baldwin, J. G. (2007). Three-dimensional fine structural reconstruction of the nose sensory structures of Acrobeles complexus compared to Caenorhabditis elegans (Nematoda: Rhabditida). *J Morphol* **268**, 649-663.

Burette, A., Collman, F., Micheva, K. D., Smith, S. J. and Weinberg, R. J. (2015). Knowing a synapse when you see one. *Front Neuroanat* **9**, 100.

Bushby, A. J., Mariggi, G., Armer, H. E. and Collinson, L. M. (2012). Correlative light and volume electron microscopy: using focused ion beam scanning electron microscopy to image transient events in model organisms. *Methods Cell Biol* **111**, 357-382.

Caplan, J., Niethammer, M., Taylor, R. M., 2nd and Czymmek, K. J. (2011). The power of correlative microscopy: multi-modal, multi-scale, multi-dimensional. *Curr Opin Struct Biol* **21**, 686-693.

Collman, F., Buchanan, J., Phend, K. D., Micheva, K. D., Weinberg, R. J. and Smith, S. J. (2015). Mapping synapses by conjugate light-electron array tomography. *J Neurosci* **35**, 5792-5807.

de Chaumont, F., Dallongeville, S., Chenouard, N., Herve, N., Pop, S., Provoost, T., Meas-Yedid, V., Pankajakshan, P., Lecomte, T., Le Montagner, Y., et al. (2012). Icy: an open bioimage informatics platform for extended reproducible research. *Nat Methods* **9**, 690-696.

Denk, W. and Horstmann, H. (2004). Serial block-face scanning electron microscopy to reconstruct three-dimensional tissue nanostructure. *PLoS Biol* **2**, e329.

Doroquez, D. B., Berciu, C., Anderson, J. R., Sengupta, P. and Nicastro, D. (2014). A high-resolution morphological and ultrastructural map of anterior sensory cilia and glia in *Caenorhabditis elegans*. *Elife* **3**.

Fuller, M. T. and Spradling, A. C. (2007). Male and female Drosophila germline stem cells: two versions of immortality. *Science* **316**, 402-404.

Hayworth, K. J., Morgan, J. L., Schalek, R., Berger, D. R., Hildebrand, D. G. and Lichtman, J. W. (2014). Imaging ATUM ultrathin section libraries with WaferMapper: a multi-scale approach to EM reconstruction of neural circuits. *Front Neural Circuits* **8**, 68.

Heymann, J. A., Hayles, M., Gestmann, I., Giannuzzi, L. A., Lich, B. and Subramaniam, S. (2006). Site-specific 3D imaging of cells and tissues with a dual beam microscope. *J Struct Biol* **155**, 63-73.

Horne-Badovinac, S. and Bilder, D. (2005). Mass transit: epithelial morphogenesis in the Drosophila egg chamber. *Dev Dyn* **232**, 559-574.

Horstmann, H., Korber, C., Satzler, K., Aydin, D. and Kuner, T. (2012). Serial section scanning electron microscopy (S3EM) on silicon wafers for ultra-structural volume imaging of cells and tissues. *PLoS One* **7**, e35172.

Hudson, A. M. and Cooley, L. (2010). Drosophila Kelch functions with Cullin-3 to organize the ring canal actin cytoskeleton. *J Cell Biol* **188**, 29-37.

Hudson, A. M., Mannix, K. M. and Cooley, L. (2015). Actin Cytoskeletal Organization in Drosophila Germline Ring Canals Depends on Kelch Function in a Cullin-RING E3 Ligase. *Genetics* **201**, 1117-1131.

Jahn, M. T., Markert, S. M., Ryu, T., Ravasi, T., Stigloher, C., Hentschel, U. and Moitinho-Silva, L. (2016). Shedding light on cell compartmentation in the candidate phylum Poribacteria by high resolution visualisation and transcriptional profiling. *Sci Rep* **6**, 35860.

Johnson, E., Seiradake, E., Jones, E. Y., Davis, I., Grunewald, K. and Kaufmann, R. (2015). Correlative in-resin super-resolution and electron microscopy using standard fluorescent proteins. *Sci Rep* **5**, 9583.

Karreman, M. A., Hyenne, V., Schwab, Y. and Goetz, J. G. (2016). Intravital Correlative Microscopy: Imaging Life at the Nanoscale. *Trends Cell Biol* **26**, 848-863.

Kasthuri, N., Hayworth, K. J., Berger, D. R., Schalek, R. L., Conchello, J. A., Knowles-Barley, S., Lee, D., Vazquez-Reina, A., Kaynig, V., Jones, T. R., et al. (2015). Saturated Reconstruction of a Volume of Neocortex. *Cell* **162**, 648-661.

Kizilyaprak, C., Daraspe, J. and Humbel, B. M. (2014). Focused ion beam scanning electron microscopy in biology. *J Microsc* **254**, 109-114.

Knott, G., Rosset, S. and Cantoni, M. (2011). Focussed ion beam milling and scanning electron microscopy of brain tissue. *J Vis Exp*, e2588.

Kolotuev, I. (2014). Positional correlative anatomy of invertebrate model organisms increases efficiency of TEM data production. *Microsc Microanal* **20**, 1392-1403.

Kolotuev, I., Hyenne, V., Schwab, Y., Rodriguez, D. and Labouesse, M. (2013). A pathway for unicellular tube extension depending on the lymphatic vessel determinant Prox1 and on osmoregulation. *Nat Cell Biol* **15**, 157-168.

Kolotuev, I., Schwab, Y. and Labouesse, M. (2010). A precise and rapid mapping protocol for correlative light and electron microscopy of small invertebrate organisms. *Biol Cell* **102**, 121-132.

Kopek, B. G., Paez-Segala, M. G., Shtengel, G., Sochacki, K. A., Sun, M. G., Wang, Y., Xu, C. S., van Engelenburg, S. B., Taraska, J. W., Looger, L. L., et al. (2017). Diverse protocols for correlative super-resolution fluorescence imaging and electron microscopy of chemically fixed samples. *Nat Protoc* **12**, 916-946.

Kremer, A., Lippens, S., Bartunkova, S., Asselbergh, B., Blanpain, C., Fendrych, M., Goossens, A., Holt, M., Janssens, S., Krols, M., et al. (2015). Developing 3D SEM in a broad biological context. *J Microsc* **259**, 80-96.

Kremer, J. R., Mastronarde, D. N. and McIntosh, J. R. (1996). Computer visualization of three-dimensional image data using IMOD. *J Struct Biol* **116**, 71-76.

Kukulski, W., Schorb, M., Welsch, S., Picco, A., Kaksonen, M. and Briggs, J. A. (2011). Correlated fluorescence and 3D electron microscopy with high sensitivity and spatial precision. *J Cell Biol* **192**, 111-119.

Lee, W. C., Bonin, V., Reed, M., Graham, B. J., Hood, G., Glattfelder, K. and Reid, R. C. (2016). Anatomy and function of an excitatory network in the visual cortex. *Nature* **532**, 370-374.

Li, X., Ji, G., Chen, X., Ding, W., Sun, L., Xu, W., Han, H. and Sun, F. (2017). Large scale three-dimensional reconstruction of an entire Caenorhabditis elegans larva using AutoCUTS-SEM. *J Struct Biol* **200**, 87-96.

Loussert Fonta, C. and Humbel, B. M. (2015). Correlative microscopy. *Arch Biochem Biophys* **581**, 98-110.

Loyer, N., Kolotuev, I., Pinot, M. and Le Borgne, R. (2015). Drosophila E-cadherin is required for the maintenance of ring canals anchoring to mechanically withstand tissue growth. *Proc Natl Acad Sci U S A* **112**, 12717-12722.

Lucas, M. S., Guenthert, M., Gasser, P., Lucas, F. and Wepf, R. (2014). Correlative 3D imaging: CLSM and FIB-SEM tomography using high-pressure frozen, freeze-substituted biological samples. *Methods Mol Biol* **1117**, 593-616.

Lucas, M. S., Gunthert, M., Gasser, P., Lucas, F. and Wepf, R. (2012). Bridging microscopes: 3D correlative light and scanning electron microscopy of complex biological structures. *Methods Cell Biol* **111**, 325-356.

Maco, B., Holtmaat, A., Cantoni, M., Kreshuk, A., Straehle, C. N., Hamprecht, F. A. and Knott, G. W. (2013). Correlative in vivo 2 photon and focused ion beam scanning electron microscopy of cortical neurons. *PLoS One* **8**, e57405.

Markert, S. M., Britz, S., Proppert, S., Lang, M., Witvliet, D., Mulcahy, B., Sauer, M., Zhen, M., Bessereau, J. L. and Stigloher, C. (2016). Filling the gap: adding super-resolution to array tomography for correlated ultrastructural and molecular identification of electrical synapses at the C. elegans connectome. *Neurophotonics* **3**, 041802.

McDonald, K. L. (2014). Rapid embedding methods into epoxy and LR White resins for morphological and immunological analysis of cryofixed biological specimens. *Microsc Microanal* **20**, 152-163.

McLaughlin, J. M. and Bratu, D. P. (2015). Drosophila melanogaster Oogenesis: An Overview. *Methods Mol Biol* **1328**, 1-20.

McLean, P. F. and Cooley, L. (2013). Protein equilibration through somatic ring canals in Drosophila. *Science* **340**, 1445-1447.

Micheva, K. D., Busse, B., Weiler, N. C., O'Rourke, N. and Smith, S. J. (2010). Single-synapse analysis of a diverse synapse population: proteomic imaging methods and markers. *Neuron* **68**, 639-653.

Micheva, K. D. and Smith, S. J. (2007). Array tomography: a new tool for imaging the molecular architecture and ultrastructure of neural circuits. *Neuron* **55**, 25-36.

Muller-Reichert, T. and Verkade, P. (2014). Preface. Correlative light and electron microscopy II. *Methods Cell Biol* **124**, xvii-xviii.

Nicolle, O., Burel, A., Griffiths, G., Michaux, G. and Kolotuev, I. (2015). Adaptation of Cryo-Sectioning for IEM Labeling of Asymmetric Samples: A Study Using Caenorhabditis elegans. *Traffic* **16**, 893-905.

Nixon, S. J., Webb, R. I., Floetenmeyer, M., Schieber, N., Lo, H. P. and Parton, R. G. (2009). A single method for cryofixation and correlative light, electron microscopy and tomography of zebrafish embryos. *Traffic* **10**, 131-136.

Noske, A. B., Costin, A. J., Morgan, G. P. and Marsh, B. J. (2008). Expedited approaches to whole cell electron tomography and organelle mark-up in situ in high-pressure frozen pancreatic islets. *J Struct Biol* **161**, 298-313.

Oberti, D., Kirschmann, M. A. and Hahnloser, R. H. (2011). Projection neuron circuits resolved using correlative array tomography. *Front Neurosci* **5**, 50.

Paez-Segala, M. G., Sun, M. G., Shtengel, G., Viswanathan, S., Baird, M. A., Macklin, J. J., Patel, R., Allen, J. R., Howe, E. S., Piszczek, G., et al. (2015). Fixation-resistant photoactivatable fluorescent proteins for CLEM. *Nat Methods* **12**, 215-218, 214 p following 218.

Paul-Gilloteaux, P., Heiligenstein, X., Belle, M., Domart, M. C., Larijani, B., Collinson, L., Raposo, G. and Salamero, J. (2017). eC-CLEM: flexible multidimensional registration software for correlative microscopies. *Nat Methods* **14**, 102-103.

Peddie, C. J., Blight, K., Wilson, E., Melia, C., Marrison, J., Carzaniga, R., Domart, M. C., O'Toole, P., Larijani, B. and Collinson, L. M. (2014). Correlative and integrated light and electron microscopy of in-resin GFP fluorescence, used to localise diacylglycerol in mammalian cells. *Ultramicroscopy* **143**, 3-14.

Pluk, H., Stokes, D. J., Lich, B., Wieringa, B. and Fransen, J. (2009). Advantages of indium-tin oxide-coated glass slides in correlative scanning electron microscopy applications of uncoated cultured cells. *J Microsc* **233**, 353-363.

Robinson, D. N., Cant, K. and Cooley, L. (1994). Morphogenesis of Drosophila ovarian ring canals. *Development* **120**, 2015-2025.

Saalfeld, S., Fetter, R., Cardona, A. and Tomancak, P. (2012). Elastic volume reconstruction from series of ultra-thin microscopy sections. *Nat Methods* **9**, 717-720.

Schindelin, J., Arganda-Carreras, I., Frise, E., Kaynig, V., Longair, M., Pietzsch, T., Preibisch, S., Rueden, C., Saalfeld, S., Schmid, B., et al. (2012). Fiji: an open-source platform for biological-image analysis. *Nat Methods* **9**, 676-682.

Schwarz, H. and Humbel, B. M. (2014). Correlative light and electron microscopy using immunolabeled sections. *Methods Mol Biol* **1117**, 559-592.

Starborg, T., Kalson, N. S., Lu, Y., Mironov, A., Cootes, T. F., Holmes, D. F. and Kadler, K. E. (2013). Using transmission electron microscopy and 3View to determine collagen fibril size and three-dimensional organization. *Nat Protoc* **8**, 1433-1448.

Sundaram, M. V. and Buechner, M. (2016). The Caenorhabditis elegans Excretory System: A Model for Tubulogenesis, Cell Fate Specification, and Plasticity. *Genetics* **203**, 35-63.

Titze, B. and Genoud, C. (2016). Volume scanning electron microscopy for imaging biological ultrastructure. *Biol Cell* **108**, 307-323.

Wacker, I. and Schroeder, R. R. (2013). Array tomography. *J Microsc* **252**, 93-99.

Wacker, I., Spomer, W., Hofmann, A., Thaler, M., Hillmer, S., Gengenbach, U. and Schroder, R. R. (2016). Hierarchical imaging: a new concept for targeted imaging of large volumes from cells to tissues. *BMC Cell Biol* **17**, 38.

Watanabe, S., Punge, A., Hollopeter, G., Willig, K. I., Hobson, R. J., Davis, M. W., Hell, S. W. and Jorgensen, E. M. (2011). Protein localization in electron micrographs using fluorescence nanoscopy. *Nat Methods* **8**, 80-84.

White, J. G., Southgate, E., Thomson, J. N. and Brenner, S. (1986). The structure of the nervous system of the nematode Caenorhabditis elegans. *Philos Trans R Soc Lond B Biol Sci* **314**, 1-340.

Table 1

Steps	Multiplex labeling	Volume reconstruction	CLEM
Fixation	HPF-QFS	OTO	HPF-QFS
Embedding resin	Acrylic	Epon	Acrylic
Sectioning and transfer	Coverslip	Silicon wafer	Coverslip or silicon wafer
Stain	1° and 2° Abs	Direct observation	Direct observation or 1° and 2° Abs
Microscope type	widefield /confocal	FEG-SEM	widefield /confocal / FEG-SEM
Destaining	0.2 M NaOH, 0.02 % SDS	NA	NA
Restain	1° and 2° Abs		UAc/Pb
Reconstruction	Fiji/3Dmod		

Table 1. A simplified summary of AT procedures with the changes in the flow necessary for three preparation strategies.

HPF-QFS: high-pressure freezing- quick freeze substitution. OTO: enhanced contrast procedure. After fixation, the embedding medium differs: hydrophilic acrylic resin is preferred when there is a need to preserve antigenicity and fluorescence signals; hydrophobic epoxy resins are used when the ultrastructure is the main goal. The microscope used depends on the imaging goal.

Figures
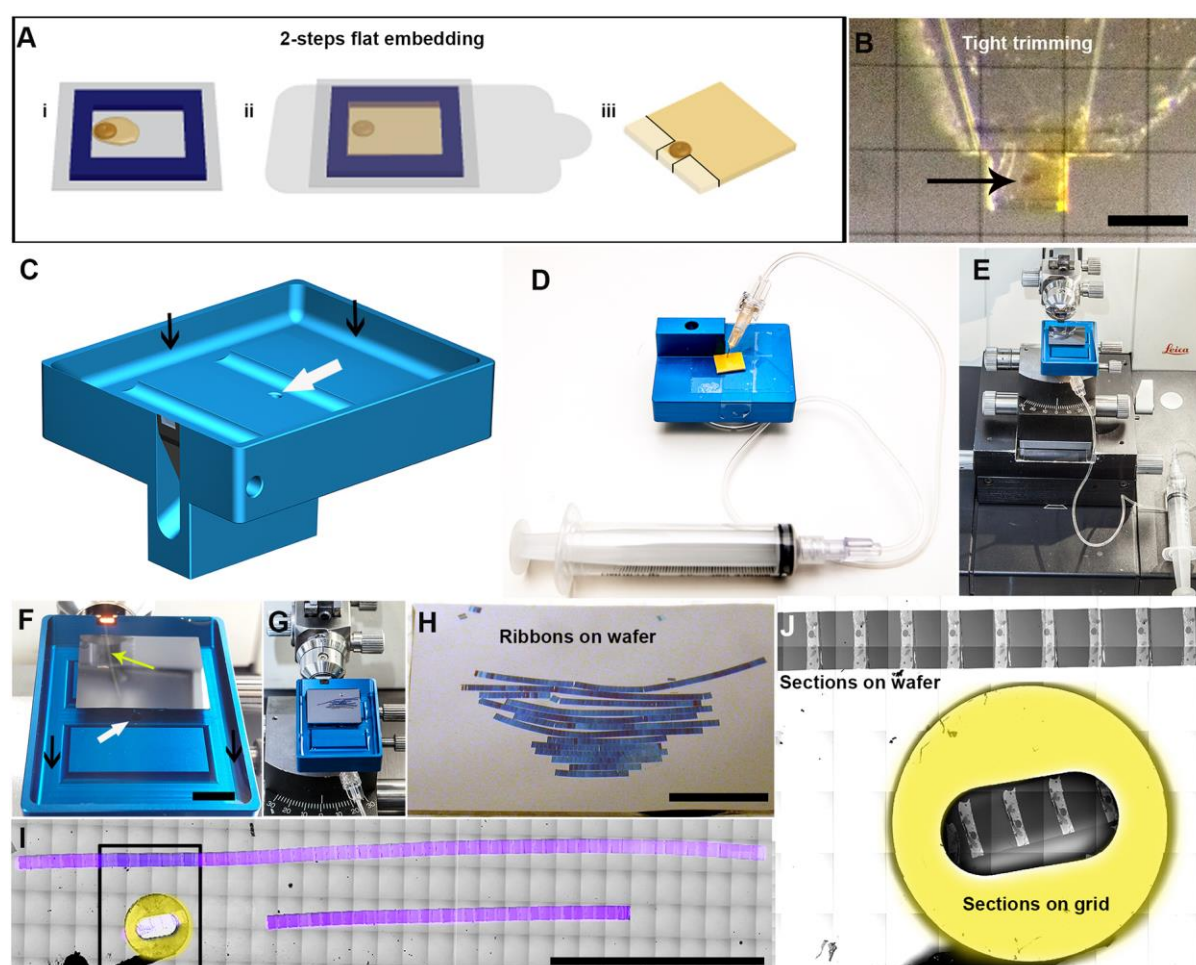
Figure 1, AT: Generation of arrays of aligned ribbons of consecutive sections

A. Two-step flat embedding procedure: Resin-infiltrated samples are pre-polymerized on the film within a frame (i). Next, the frame is filled with resin and set to polymerize completely (ii). These flat blocks can be directly sectioned without further re-embedding, allowing rapid localization of the samples. Black lines outlining the bright zones show the area dedicated for the trimming (iii).

B. Tight trimming of the sample with the 90º diamond trim knife: The sample is oriented in the middle of resin support (arrow) and the surrounding resin tightly trimmed. This step minimizes the amount of resin around the sample, reducing the surface area of each section, and maximizing the number of sections that can be accommodated on one microscope slide or wafer. Scale bar, 200 µm.

C. A drawing of a modified AT-boat diamond knife enlarged and flattened to facilitate sectional collection on glass or wafer support. As part of the modifications, we carved water evacuation ditches (black arrows) and drilled a hole (white arrow) in the bottom of the boat.

D. A syringe needle is connected to the hole and covered with double-sided sticky tape. A catheter tube connects it to a syringe. The internal diameter of the needle determines the speed of water retraction. Thus, water can be retracted, or drained, from below the water surface, either actively, using the syringe, or passively, by allowing water to drip at a steady pace through the catheter, leaving both hands of the operator free to align sections on the support.

E. A complete description of tasks necessary for array generation: the modified AT diamond knife is connected to a syringe and installed on the ultramicrotome. Before sectioning, the support (a coverslip or wafer) is entirely submerged in water and lies parallel to the water surface.

F. A ribbon of consecutive sections floating inside the modified boat while sectioning (yellow arrow). A rectangular wafer lies on the bottom of the boat. Scale bar, 1 cm.

G. After sectioning, the ribbons of consecutive sections are aligned side by side, and water is gradually drained from the boat. After either assisting with a syringe or allowing the water to drain away completely, the support remains at the bottom of the boat until any remaining moisture has evaporated completely from its surface (Movie 1).

H. Aligned ribbons of consecutive sections transferred to wafer support. Scale bar, 1 cm.

I. A stitched montage of multiple light microscopy images acquired with the CorrSight, that covers sections transferred on wafer. 115 sections (pseudo colored in purple) on a wafer versus three on the TEM grid. Scale bar 10 mm.

J. An inset with the stitched SEM images acquired with the MAPs interface cover part of the wafer and a TEM grid with the sections from the same preparation. Scale bar 10 mm
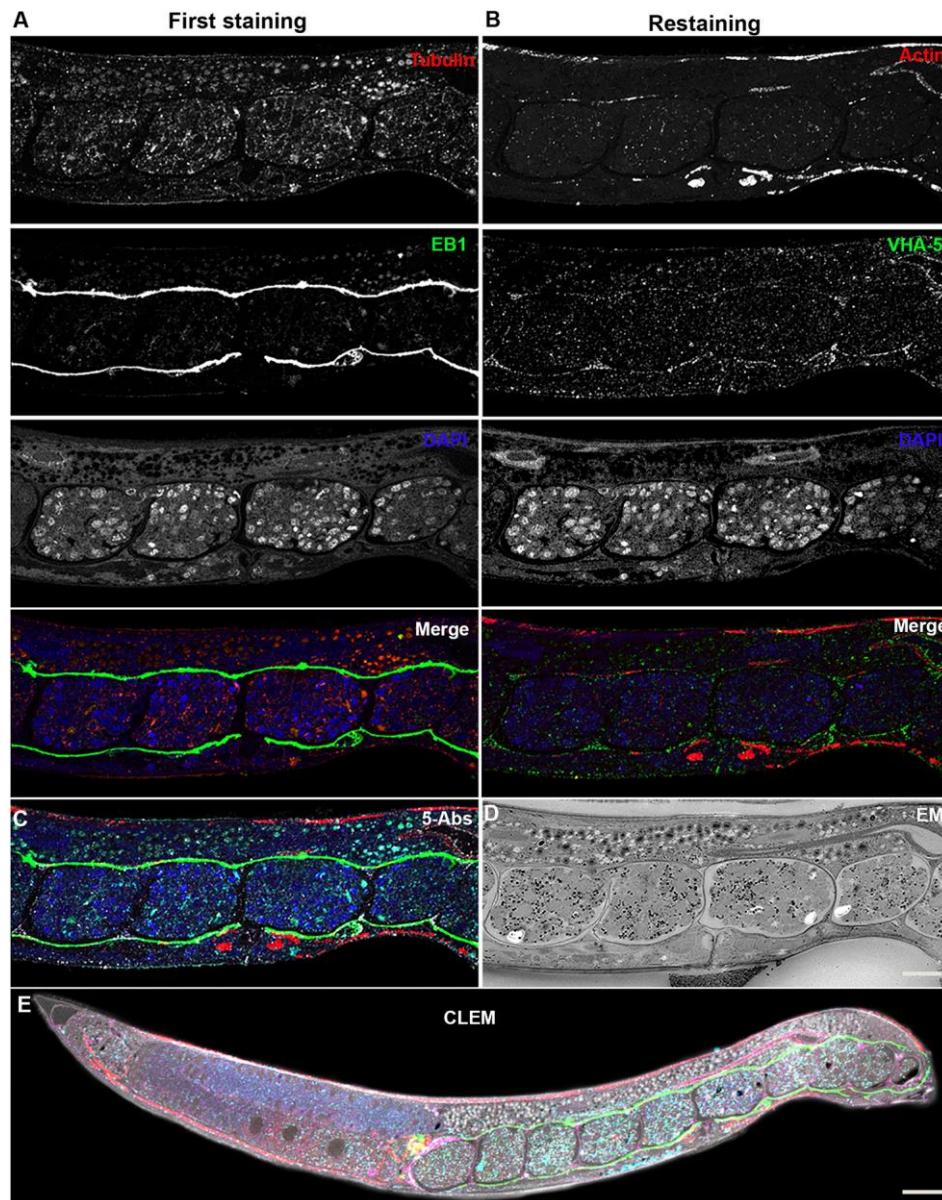
Figure 2. Light microscopy and multiplex imaging: immunolabeled *C. elegans* sections on coverslips

A. Merge of 25 fluorescently-labeled longitudinal oriented sections through the middle portion of a *C. elegans* adult (tubulin – red, EB1 – green, DAPI – blue), and overlap of all three channels (merge).

B. Immunolabeling the same sections after eluting the initial labeling, washing, and re-labeling with a second set of markers (actin – red, VHA-5 – green, DAPI – blue). DAPI nuclear staining served as an alignments reference to combine the first and second datasets.

C. Merged image of both labeling rounds, labeling all five markers (tubulin – red, EB1 – green, actin – red, VHA-5 – green, DAPI – blue).

D. An inverted contrast SEM image of one section from the middle of the array that corresponds to the labeled region (vulva and embryos).

E. Superposition of the quintuple immunolabeling and the EM image over the entire zone of sectioning. (Movie 2).

Scale bar, 10 µm in all images.
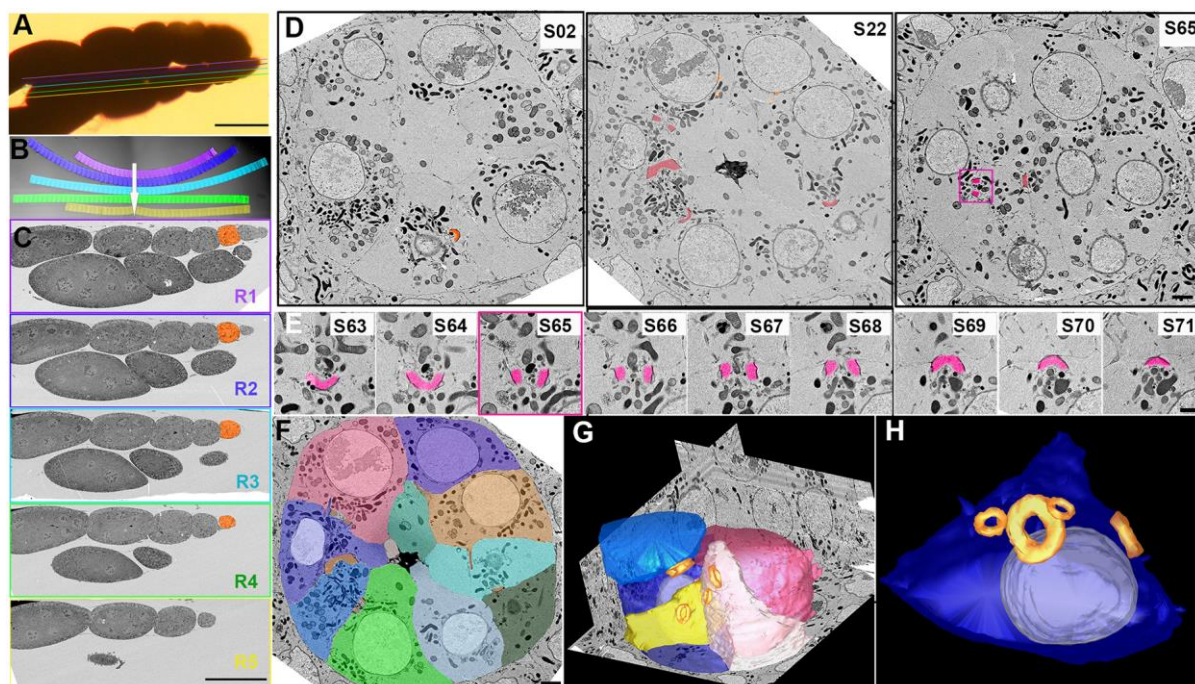
Figure 3. Blind screening approach for morphological analysis and 3D reconstruction of AT data

A. Image of *Drosophila* ovarioles flat-embedded in epon resin and arranged for sectioning. Line colors designate an approximate region of sectioning (Panels B, C). Scale bar, 100 µm.

B. Sections collected on wafer support. Each row is color-coded to correspond to the colored lines in Panel A. Scale bar 1 mm.

C. SEM image of "lateral low magnification screening" strategy: Horizontally "leaping" from one ribbon of consecutive sections to another helps to rapidly reveal the region of interest (ROI) in the sample, based on previous knowledge of anatomy. In this case, the ROI is the stage 3 ovarian chamber (orange), and the sections in ribbons 4 and 5 do not merit further study. Scale bar 100 µm.

D. Selected images of low magnification screening aimed at localizing the ROI: ring canals (highlighted in magenta). Ring canals are randomly scattered inside the ovarian sphere in random orientations and have distinct morphological characteristics. Locating ring canals by analyzing serial sections is tedious and often not successful. Rapid screening, in contrast, successfully facilitates this task. The magenta box encircles the canal we aimed to analyze more precisely. Scale bar, 2 µm. (Movie 3).

E. High magnification SEM analysis of a single ROI, a ring canal (pseudo-colored in magenta). Section 65 (S65) – the same zone as in panel E is highlighted in magenta. (Movie 4). Scale bar, 1 µm.

F. A selected SEM image from the image sequence colored using the IMOD program (Movie 5).

G. Volume reconstruction of sections from the image stack. Cell boundaries are represented by different colors; nuclei – white; ring canals - orange.

H. A subset of the rendering dataset. Future oocyte interconnected with the nurse cells through four ring canals (cell contour – blue; nucleus – white; ring canals - orange).
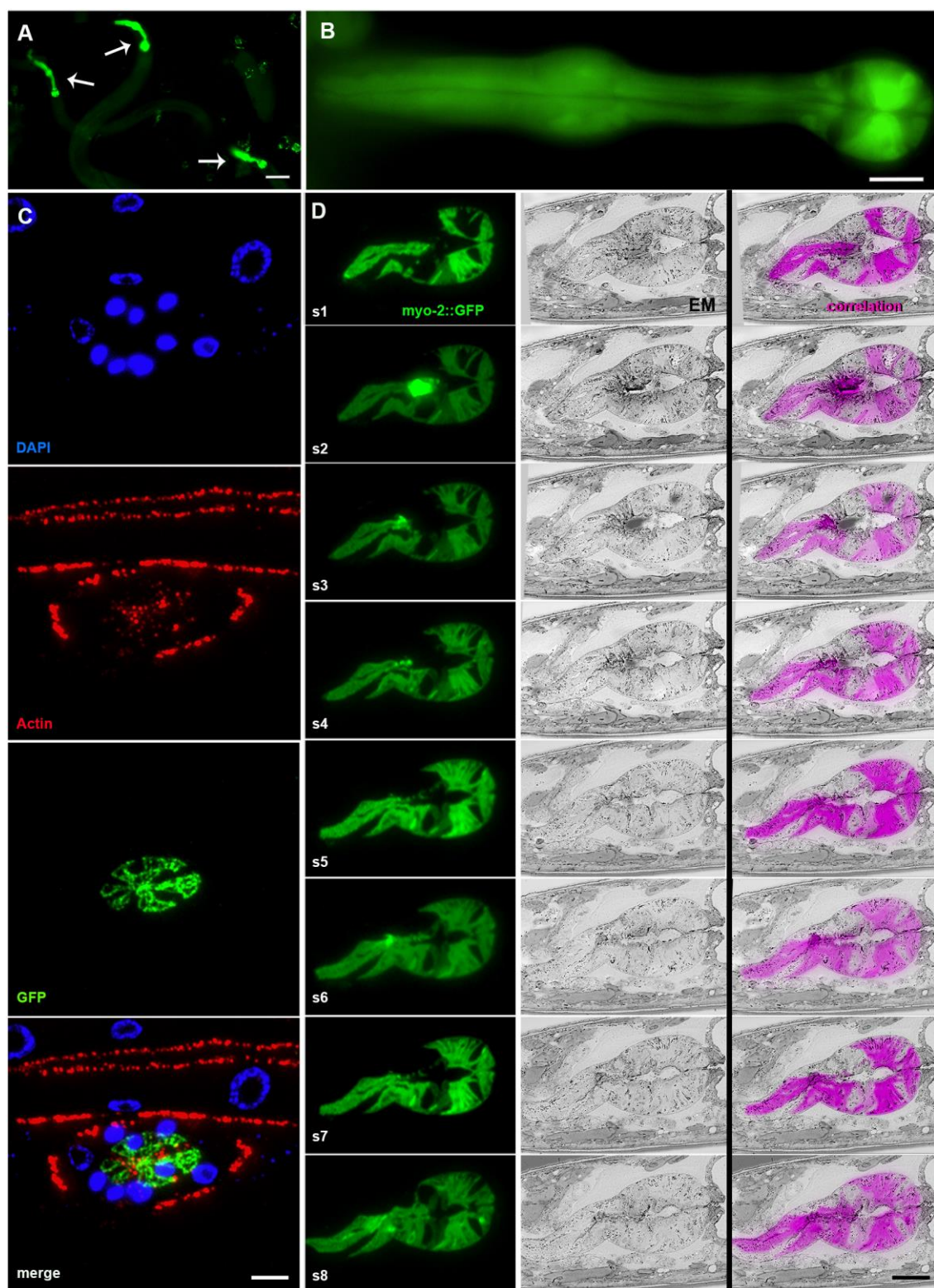
Figure 4. *In vivo* fluorescence retention for CLEM

A. *In-resin* fluorescent image of embedded *C. elegans* larvae with *myo-2::GFP* fluorescence signal in the pharynx (arrows indicate individual larvae). Scale bar, 10 µm.

B. Fluorescent image of the *C. elegans* pharynx labeled with *myo-2::GFP*, embedded in hydrophilic HM20 resin. Scale bar, 10 µm.

C. Immunolabeling of sections through the transversely sectioned pharyngeal region of a *C. elegans* larva: The retained GFP signal (green) and additional labeling (actin for muscles – red, nuclei stained with DAPI – blue) can be seen, with 25 sections aligned and merged. Scale bar, 10 µm.

D. 3D-correlated panel of eight consecutive longitudinal sections through the pharyngeal region of a *C. elegans* larva*: myo-2: GFP* (green), inverted SEM (grey) and the merge of both types of images (GFP signal inverted to magenta for better visualization). Scale bar, 10 µm.
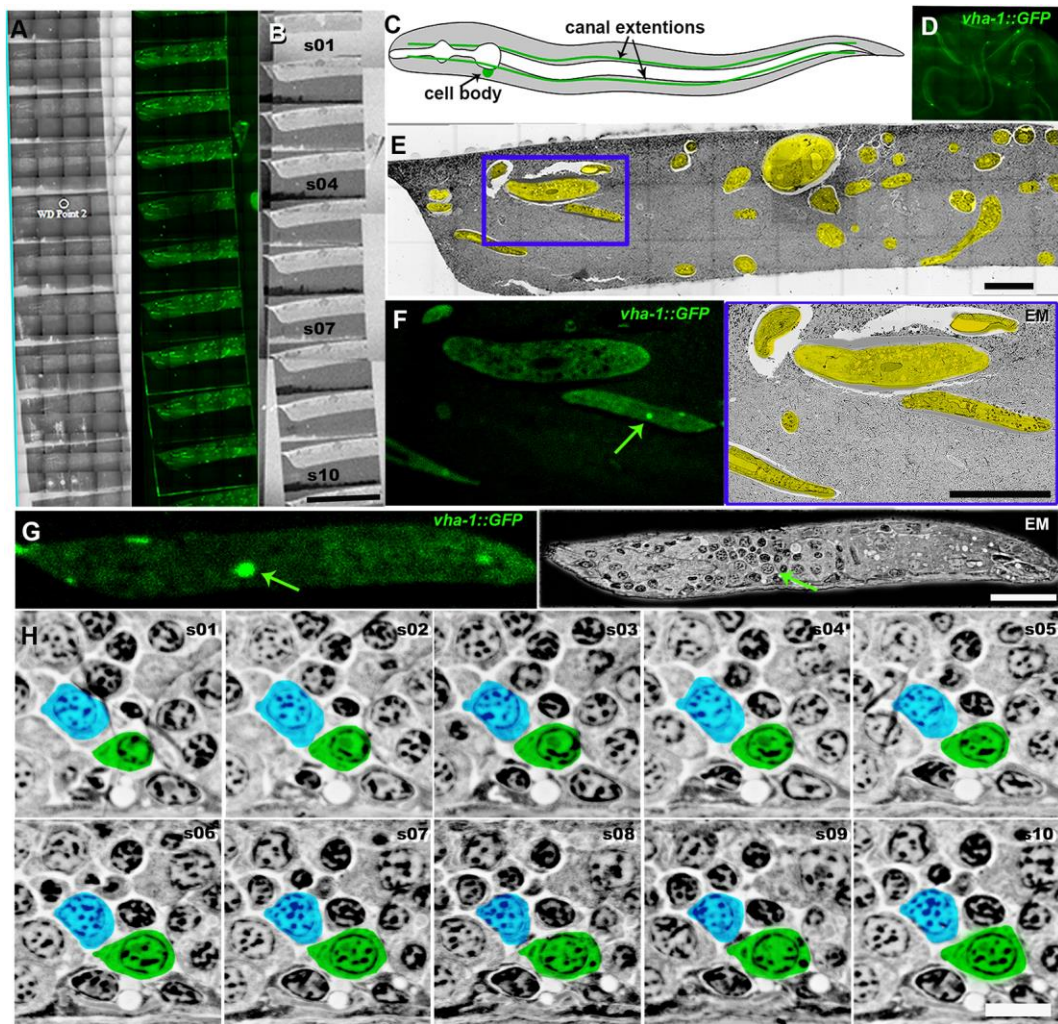
Figure 5. MAPS mediated screening strategy: *C. elegans* excretory canal

A. An array of sections on a wafer visualized by the light microscopy reflection mode and GFP-signal visualized by CorrSight MAPs based tiles acquisition. Scale bar, 500 nm.

B. The same array visualized with the BSE-SEM. Scale bar, 500 nm.

C. A schematic representation of the *C. elegans* excretory canal (green) with the cell body and four lateral tubular extensions.

D. *C. elegans vha-1::GFP* larvae embedded in hydrophilic HM20 resin after high-pressure freezing-rapid freeze substitution. Excretory canal fluorescence is preserved.

E. An EM image of a representative section on a wafer acquired with SEM-BSE detector at low magnification. Numerous *C. elegans* samples present in this section are highlighted in yellow. This overview of the content of the section can help during pre-screening of multiple

sections before starting the EM part of CLEM analysis. The blue box designates the portion of the image represented in panel F. Scale bar, 50 µm.

F: An inset from Panel E. GFP image of *vha-1::GFP* labeling of the excretory canal on the section and the same area visualized with BSE-SEM (green arrow to highlight the excretory canal cell body). Scale bar, 10 µm.

G. A side by side fluorescence and EM image of the sample from Panel F. The arrow points to the excretory cell body. Scale bar, 10 µm.

H. A sequence of inverted SEM images of the excretory canal cell from the subsequent sections. The excretory cell was colored in green, a random neighbor cell was colored in blue. Note that the cells surrounding the labeled cells appear identical, and in the absence of the superposition, it could be impossible to recognize the cell of interest. Scale bar, 5 µm.
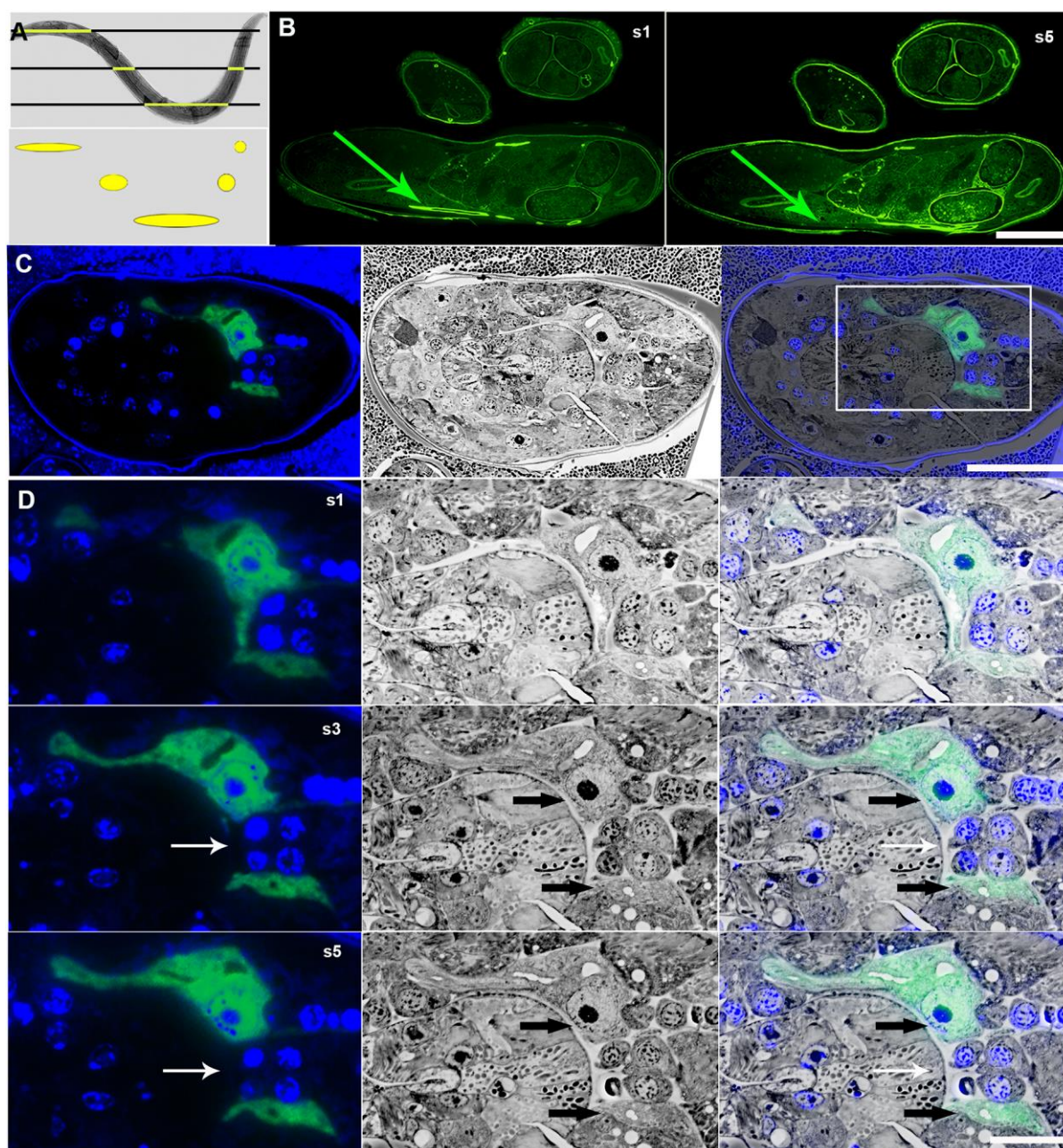
Figure 6. AT of nonlinear sample

A. A *C. elegans* larva embedded in hydrophilic HM20 resin to illustrate the result of ultrathin sectioning, and diagram the outcome of the sectioning. Note that on the section, the same animal might appear as two independent samples if it is sectioned in the upper part.

B. Fluorescence images of two random fluorescent sections spaced by 500 nm of the excretory canal GFP signal on five different sections. Scale bar, 50 µm.

C. An oblique section of a *C. elegans* larva at the level of excretory canal cell body: *vha-1*::GFP, BSE-SEM and merge image. The white box designates the position of panel D. Scale bar, 10 µm.

D. Representative sections of the excretory canal cell body of a *C. elegans* larva and its lateral extensions. The white arrow points to the disappearing part of the canal, leaving two parts that without the fluorescent context might be difficult to recognize on EM micrograph (black arrows). Scale bar, 2 µm.

Supplementary Figure 1
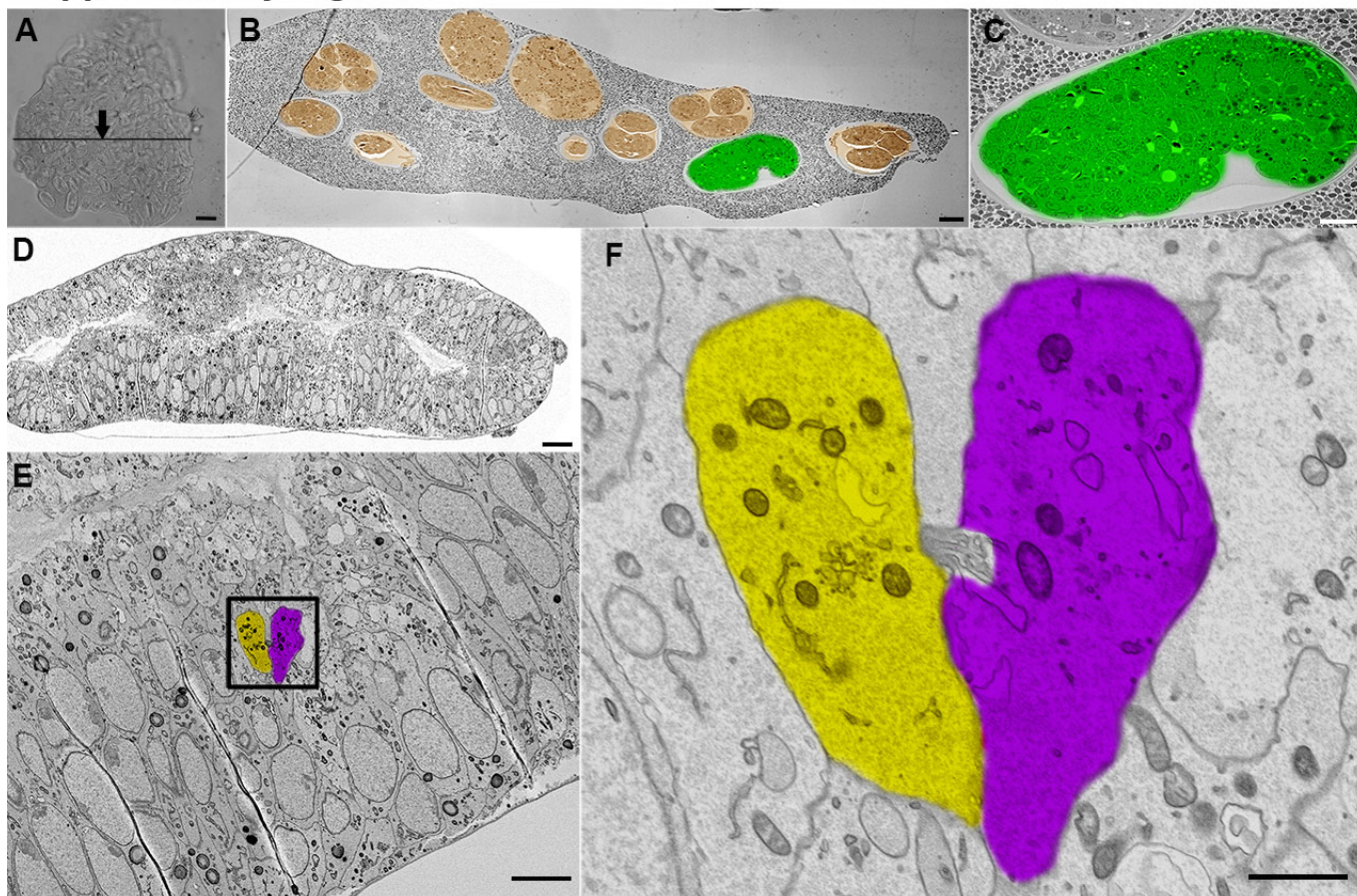
Figure S1. Examples of AT-assisted analysis of different complex samples

A. "Blind screening" of *C. elegans* embryos: A resin block containing a pellet of mixed stage embryos randomly sectioned through the area designated by the black line. Scale bar, 50 µm.

B. Low-magnification SEM-BSE image of a section from Panel A (black line). Embryos at various stages are pseudo-colored in orange, and a 1.2-fold stage embryo in the desired orientation is colored in green. Scale bar, 10 µm.

C. High-magnification image of the embryo of interest (Panel B). Rapid AT screening will provide sufficient embryos at the desired stage for the operator to choose the desired orientation, based on previous knowledge of the anatomy of the specimen. Thus, sample orientation is unnecessary. Scale bar, 5 µm.

D. SEM section through a *Drosophila* larval wing disc. Scale bar, 10 µm.

E. High magnification of epithelial cells within the wing disc (Panel D). Cell division events are frequently studied in the *Drosophila* wing disc in fixed tissue processed for TEM. Locating the event of cell abscission and retrieving the complete volume of both dividing cells is technically challenging. Quick screening of multiple regions in numerous rows of sections facilitates this operation, allowing the timely location of the desired area. Scale bar, 2 µm.

F. High magnification view (Panel E): two cells (yellow and purple) at the end of cell division, in telophase, with the cellular bridge still connecting both cells. Scale bar, 1 µm.
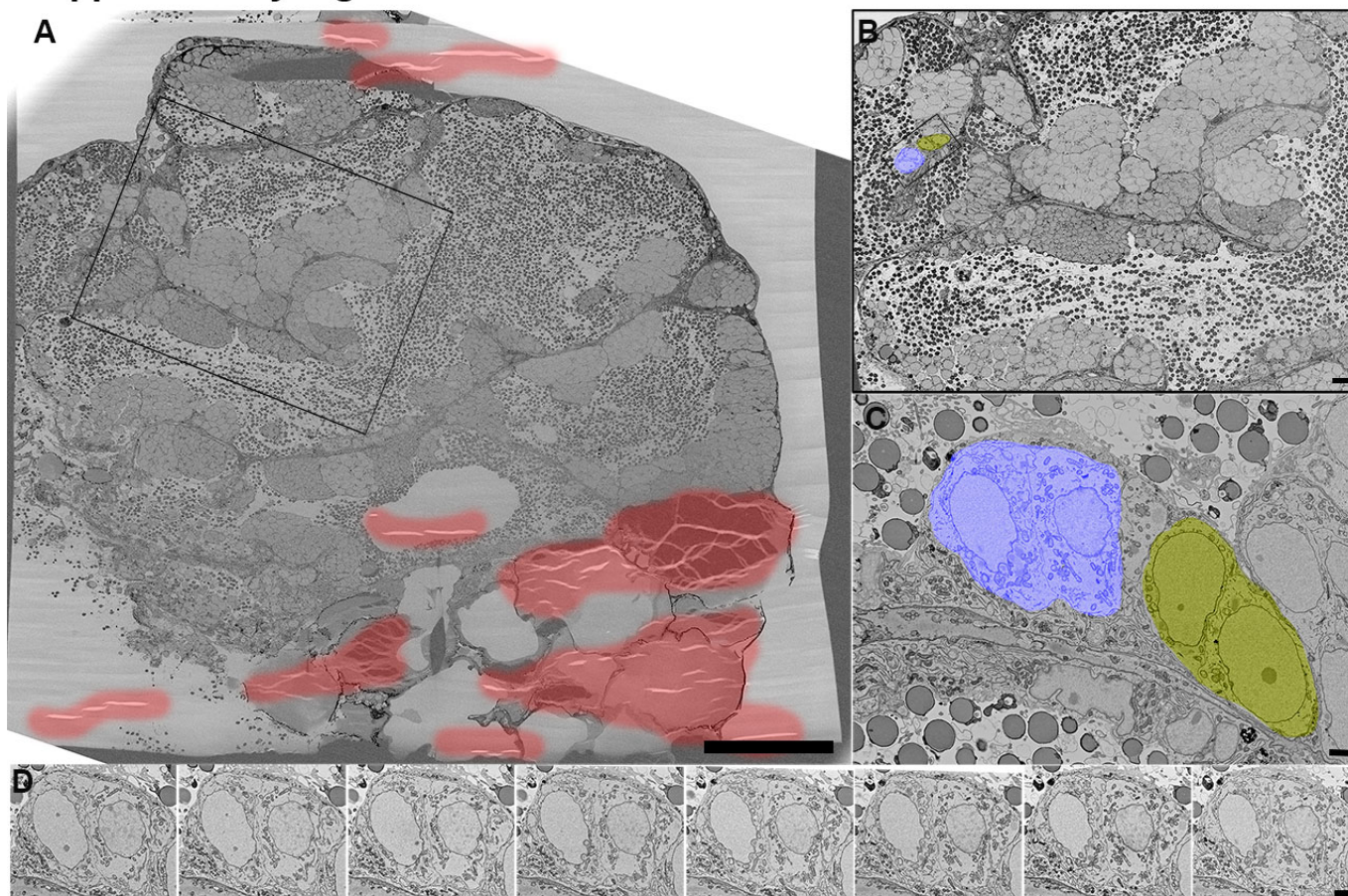
Supplementary Figure 2

Figure S2. Examples of AT-assisted analysis of different complex samples

A. Low magnification view on a section an SEM image of a cross-section through a zebrafish testis. The regions containing the folds/microfolds are highlighted in red. Scale bar 100 µm.

B. Higher magnification on the global area of interest (black rectangle in Panel A) that contains no wrinkles. The structure is composed of cell clusters (cysts) at various stages of cell division. The mother cells that initiate such clusters by undergoing multiple rounds of cell division are randomly scattered throughout the spermatheca. Our AT approach with "blind" sectioning greatly facilitates locating the mother cells compared with standard sectional analysis. Black box encircles a potential ROI. Scale bar, 10 µm.

C. Close-up of two pairs of precursor cells highlighted in blue and in yellow (Box in Panel G). After a single section containing the ROI has been identified by "horizontal" screening (Figure 4C), the sections sequentially upstream and downstream of the initially identified section (i.e., "vertical") within the same ribbon of consecutive sections can be analyzed. Scale bar, 2 µm.

D. A sequence of serial images obtained from the blue area (Panel G). None of the sections was affected either by the folds or the microfolds. Scale bar 2 µm.
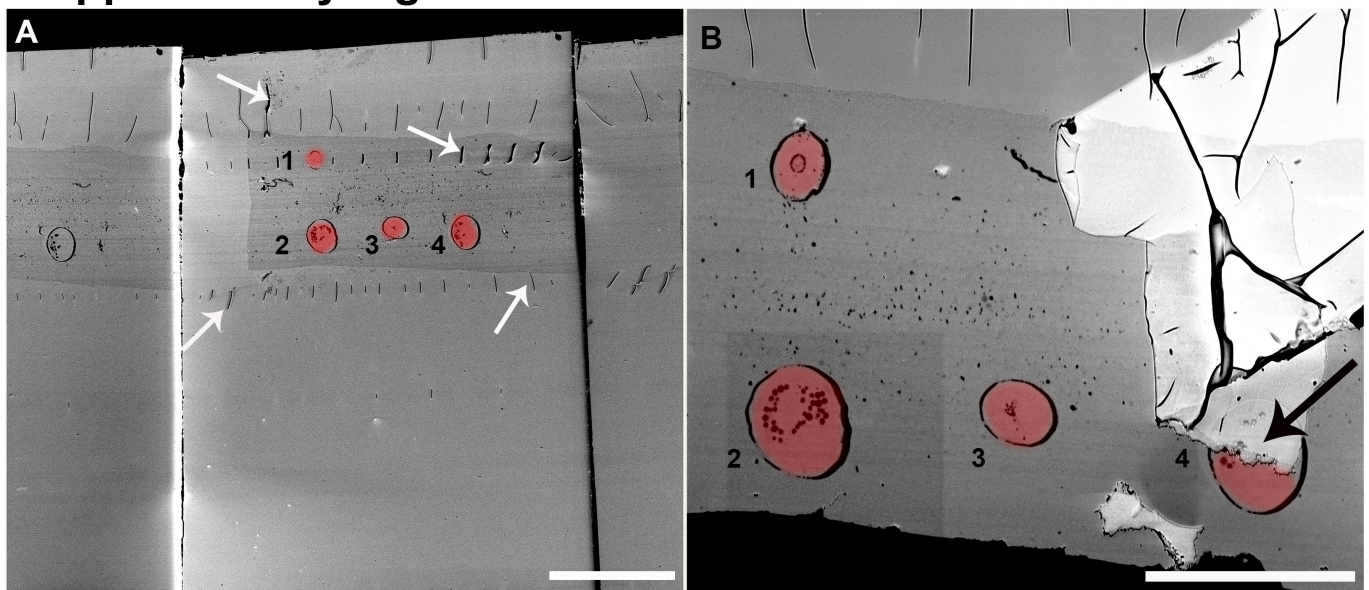
Supplementary Figure 3

Figure S3. An example of the folds and micro folds on sections

A. An overview of several ribbons of consecutive sections on a wafer. Four *C. elegans* larvae, randomly cut through the body are shown. Arrows point to some microfolds. Scale bar 100 µm.

B. An example of a severe damage on section. Part of the resin from another section has landed on the adjacent section, partially ruining it (arrow). Scale bar 50 µm.
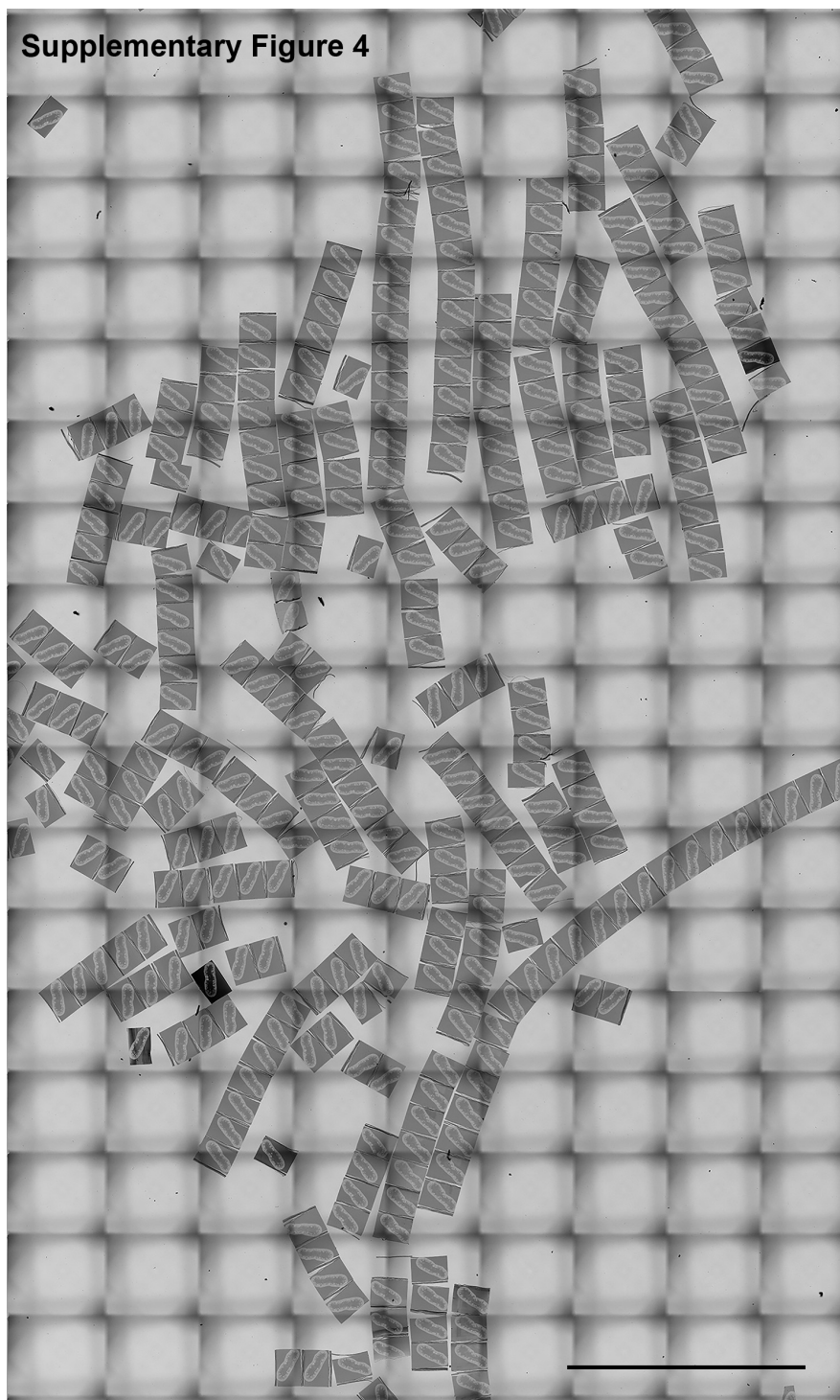
**Figure S4. Scattered sections collected on wafer in a random orientation**

Drosophila gut sections transferred on the wafer. Multiple low magnification tiles stitched together. An example of particularly unsuccessful sectioning and arrays alignment. Sections are scattered in all directions and even in this severe case there are few to none folds on sections. The image can be zoomed in to see the details. Scale bar 500 µm.

Supplementary Movies

Movie 1. Sectioning and on-wafer transfer of the arrays using the modified diamond knife with the modified basin. There are several key steps in this procedure:

1. Sectioning. The time required for sectioning depends on the desired number of sections and the speed of sectioning. We used a rate of 0.8-1.0 μm/sec.

2. Alignment of ribbons of consecutive sections. During the first step, one or several ribbons can be generated. Multiple ribbons can be arranged side by side using gentle movements of an eyelash attached to a thin stick.

3. Water draining. Water retraction can be achieved by active aspiration through the syringe and by passive dripping through the plastic catheter. The entire procedure takes a couple of minutes at the most.

4. Readjustment of ribbons. While draining the water from the basin, the aligned ribbons often become misaligned. While water remains on the surface of the wafer, we can readjust the ribbons until the surface starts to dry.

5. Gradual evaporation of water from the surface of the wafer. We consider this step to be critical to avoid folds in the sections. The visual zoom-in on a drying portion of the ribbon illustrates this concept well. The length of time for drying will largely depend on the size of the surface area and the surrounding environmental conditions. In practice, drying takes 10 to 30 minutes for a wafer of 2x4 cm.
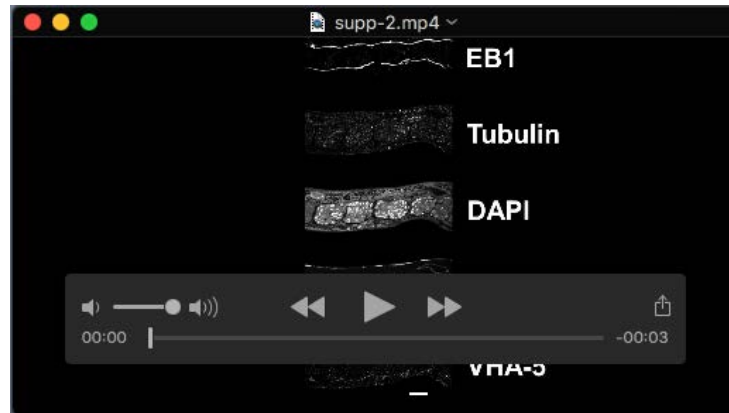
Movie 2. Alignment of the sequences of the labeled sections presented in Figure 2.
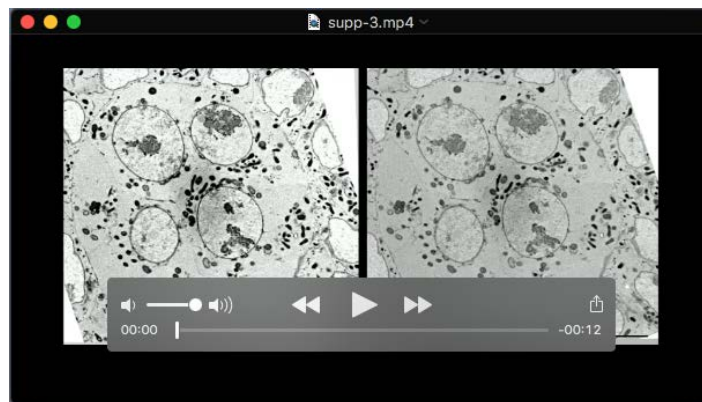
Movie 3. Alignment of multiple SEM-BSE images of sections through *Drosophila* ovarian chamber. All ring canals are pseudo-colored in orange with the selected ring in magenta. Side by side representation of the on-surface tracking (left) and a 3D ring canals rendering model (right).
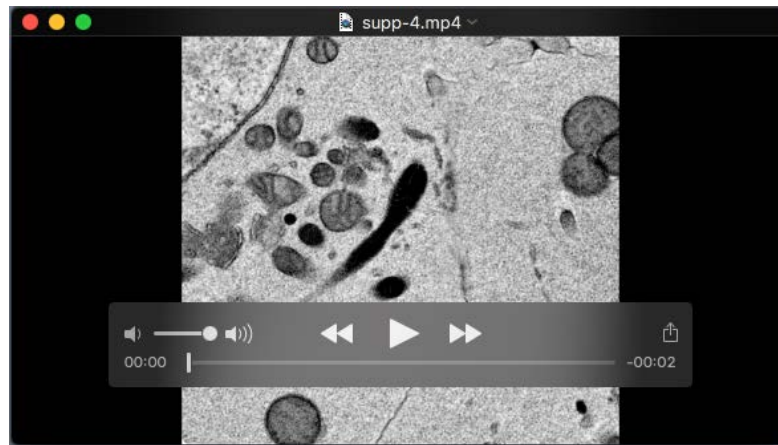
Movie 4. Close-up of a ring canal from the dataset presented in the Movie 3, colored in magenta, captures with using higher-resolution SEM-BSE acquisition parameters.
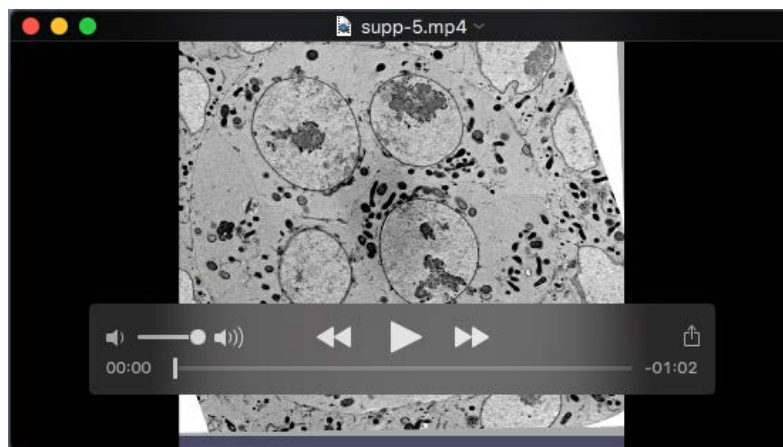
Movie 5. Modeling and rendering data set of multiple SEM-BSE images of sections through a *Drosophila* ovarian chamber. An IMOD reconstruction of 80 sections featuring cells labeled in various colors as well as their interactions, and the connections through the ring canals (yellow).

```
macro register_tomo_fluo{
        Dialog.create("Register tomo fluo");
        Dialog.addChoice("Macro", newArray("Split Stack", "Register Reference", "Apply
transformation"));
        Dialog.show();
        macroChoice = Dialog.getChoice;

        if (macroChoice == "Split Stack"){

                // params
                Dialog.create("Channel number");
                Dialog.addNumber("Channel number", 3);
                Dialog.show();
                channelNumber = Dialog.getNumber;

                // input image
                var inputImageID = getImageID();
                var inputImageTitle = getTitle();
                print("tomo");getDimensions(width, height, channels, slices, frames);print("tomo1");
                var slicesNb = slices;
                var imageMaxSize = maxOf(width, height);

                // parameters values
                var outputDir = getDirectory("Choose a Directory");

                // split the channels to individual files
                for(c =1 ; c <= channelNumber ; c++){
                        File.makeDirectory(outputDir + "C" + c);
                }

                splitStackToImages(channelNumber);
        }
        else if(macroChoice == "Register Reference"){

                // get parameters
                Dialog.create("Register tomo fluo");
                Dialog.addChoice("Reference channel", newArray("C1", "C2", "C3", "C4", "C5", "C6"));
                Dialog.addNumber("Registered Iage Size", 1024);
                Dialog.show();
                var referenceChannel = Dialog.getChoice;
                var imageMaxSize = Dialog.getNumber;
                var outputDir = getDirectory("Select the Directory containing the Cx input images
folder");

                // register reference stack
                File.makeDirectory(outputDir + "reg_C1");
                File.makeDirectory(outputDir + "reg_C2");
                File.makeDirectory(outputDir + "reg_C3");
                File.makeDirectory(outputDir + "reg_C4");
                File.makeDirectory(outputDir + "reg_C5");
```

```
                File.makeDirectory(outputDir + "reg_C6");
                File.makeDirectory(outputDir + "reg_transform");
                register_reference();
        }
        else if(macroChoice == "Apply transformation"){

                var outputDir = getDirectory("Choose a Directory");
                applyTranformation();
        }
}

function splitStackToImages(channelNumber){

        //run("Stack to Hyperstack...", "order=xyczt(default) channels=3 slices="+slicesNb/3+" frames=1
display=Color");
        run("Split Channels");

        for (c = 1 ; c <=channelNumber ; c++){
                selectWindow("C"+c+"-" + inputImageTitle);
                run("Image Sequence... ", "format=TIFF save=["+outputDir + "C"+c+"\\C"+c+"-
0000.tif]");
        }
}

function register_reference(){

        run("Register Virtual Stack Slices", "source="+outputDir+referenceChannel +
          " output="+outputDir+"reg_"+referenceChannel +" feature=Rigid
registration=[Rigid            -- translate + rotate              ]" +
          " advanced save initial_gaussian_blur=1.60 steps_per_scale_octave=3
minimum_image_size=64 maximum_image_size="+imageMaxSize+" "+
          " feature_descriptor_size=8 feature_descriptor_orientation_bins=8
closest/next_closest_ratio=0.92 maximal_alignment_error=25 "+
          " inlier_ratio=0.05 feature_extraction_model=Rigid registration_model=[Rigid            --
translate + rotate           ] interpolate");

}

function applyTranformation(){

        for(c = 1 ; c <=6 ; c++ ){
                channel = "C"+c;
                args = "source="+outputDir + channel+" output="+outputDir+"reg_"+channel+"
transforms="+outputDir+"reg_transform"+" interpolate";
                run("Transform Virtual Stack Slices", args);
        }
        run("Merge Channels...", "c1=[Registered C1] c2=[Registered C2] c3=[Registered C3]
c4=[Registered C4] c5=[Registered C5] c6=[Registered C6] create");
        Stack.setDisplayMode("color");
        saveAs("TIFF", outputDir + "reg_stack.tif");
}
```